POLITECNICO DI TORINO

Master's Degree in Aerospace Engineering

Experimental investigation of the aeroacoustic performance of shrouded propeller systems

Supervisors:
Prof. Francesco Avallone
Prof. Chaitanya Paruchuri

Candidate:
Jona Ballgjati

December 2024

Abstract

In recent years there has been a growing interest towards Unmanned Aerial Vehicles (UAVs), however the noise they generate is still an obstacle to their widespread acceptance. Several propulsion configurations have been assessed to tackle this problem, and a substantial research effort is directed towards shrouded propeller systems. This paper presents an experimental study on the effects of duct length on noise propagation. Acoustic measurements are taken both in the far-field and from inside the duct, offering an insight into the near-field sound propagation. The microphones inside the duct allow us to study how the sound level is distributed both along the axial direction and across the azimuthal angle. This enables us to identify the frequency ranges of interest and evaluate how sound waves propagate within these shrouded systems. Two different ducts, differing in length but with identical intake geometry, are tested and compared. These tests highlight that a non aerodynamically-optimized lip intake shape, and the presence of the shroud alters the inflow characteristics into the propeller and thus its noise sources. Sound pressure measurements were complemented by Hot-Wire measurements of the velocity field, which revealed a strong boundary layer separation. Among the results obtained, it was found that the longer duct generates higher broadband noise in the far field compared to the short duct configuration. Various hypotheses have been proposed to explain this behavior, with the primary cause believed to be the asymmetrical position of the source within the duct, which may have caused constructive interference between the waves propagating downstream and upstream the duct. The long hard-walled duct configuration is chosen as the baseline to assess the impact of introducing an Over-Tip-Rotor grooved metal foam liner inside the duct.

Contents

List of Figures

List of Tables

Chapter 1

Introduction

1.1 State of the Art

In recent years there has been a growing interest towards Unmanned Aerial Vehicles (UAVs). They play a central role in a wide array of industries, with examples in the medical sector, search and rescue operations and parcel delivery services. While they are attractive thanks to several of their characteristics, such as cost-efficiency and manoeuvrability, the noise they generate is still an obstacle to their widespread acceptance. On most UAVs the propeller is typically the most dominant source of noise, producing both tonal and broadband noise Sinibaldi and Marino, 2013.

Romani et al., 2022 presented a computational approach to predict the aerodynamic performances and tonal/broadband noise radiation associated to a two-bladed propeller operating at low Reynolds numbers.

It is shown by Rizzi, 2020, that due to the lower blade tip velocity of small-scale propellers, broadband self-noise becomes a relevant contributor to the far-field acoustics in addition to steady/unsteady loading and thickness noise. Consequently, considerable effort has been devoted to exploring different strategies for propeller noise reduction, including varying the blade shape and propeller layout Serré et al., 2019,Treuren and Wisniewski, 2019.

Another topic of interest, explored by Petricelli et al., 2023, was the effect of non-uniform flow conditions on propeller noise, leading to significant levels of noise generation due to interaction with the leading edges of the propeller blades. Several propulsion configurations have been assessed to tackle this problem, and a substantial research effort is directed towards shrouded propeller systems. Ducted propellers are an interesting design choice for unmanned aerial vehicle concepts due to a potential increase of the propeller efficiency; UAVs operate at low Reynolds numbers, meaning that the viscous effect are predominant, which decreases the

efficiency of the propellers. Therefore, a ducted propeller is a common solution to increase the efficiency of the propulsion system. Additionally, ducts provide protection by containing the blade in the event of blade failure.

A recent experimental study Yilmaz et al., 2015 has shown the favourable effect of different duct geometries on the aerodynamic performance of propellers for low advance ratio.

Further studies were made by Malgoezar et al., 2019. Two types of sources were considered and the effect of an incoming flow was also assessed. For both the omni-directional and the propeller source, in hover condition, it is found that the insertion of a duct drastically changes the way noise propagates. This means that using measurements for the unducted case will not provide relevant information for the case with the source placed inside the duct. Instead, in the presence of an incoming flow, the behaviour from the unducted and ducted case are highly similar.

Simon et al., 2023 studied the acoustic radiation from a ducted propeller in static conditions using an acoustic finite element model. The study demonstrated that the best attenuation is achieved when the propeller is centered axially in the duct, maximizing in this way the destructive interference between upstream and downstream radiated waves.

A further important contribution to the comprehension of the phenomena occurring when a propeller is placed within a duct was made by Go et al., 2023. It is found that the time-average rotating pressure field on the inner surface of the shroud close to the plane of the propeller, also makes a significant contribution to the tonal noise at the harmonics of the blade passing frequency. The interference between the noise radiated from the propeller and the shroud significantly affects the total acoustic field. Furthermore, it is shown that the introduction of a duct leads to a decrease in tonal noise levels for observers positioned downstream of the propeller, when compared to an isolated propeller.

The aim of this project is to continue the work carried out by Palleja-Cabre et al., 2024. Part of their project was dedicated to investigating the impact of two different intake geometries on noise propagation, a bellmouth and a 'lip' or unflanged intake geometry. Some of the conclusions in Palleja-Cabre et al., 2024 have shown that the intake geometry has a significant impact on the generation of noise, which is likely caused by different inflow conditions onto the propeller. Among these are enhanced propeller boundary layer/turbulence interaction noise and inflow distortion. They also investigated the performance of traditional Single-Degree-of-Freedom (SDOF) liners and grooved metal foam liners in reducing noise from shrouded propellers.

In this thesis, we carried out the evaluation of another relevant variable of the system, the effect of duct length on the propagation of noise. The studies

shown by Palleja-Cabre et al., 2024 highlight that the configuration with the unflanged intake is the least favourable, without considering any acoustic treatment, providing an increase of broadband noise of almost $20dB$ with respect to the configuration with the bellmouth intake. The intake geometry for our experiments was chosen based on the criterion of system simplicity. The experiments that were taken in this work are designed to enable future comparison with numerical data. To simplify the real-world system configuration, which will need to be reproduced for numerical calculations, a lip intake was chosen.

1.2   Noise Sources in Ducted Propellers

In this section, we present the main sources of noise that can arise in our setup. The definitions introduced in this section are based on various books: Glegg and Devenport, 2017, Munjal and Munjal, 2014 and Rienstra, n.d.

1.2.1   Propeller Noise

Rotating blades generate two distinct types of acoustic signatures. The first type, known as tonal or harmonic noise, arises from sources that repeat identically with each rotation. The second type is broadband noise, a random and non-periodic signal resulting from turbulent airflow over the blades. Unlike harmonic noise, a typical broadband signal lacks periodicity but exhibits an envelope that changes periodically. To evaluate the relative significance of tonal and broadband noise, examining the narrow-band frequency spectrum of the signal is crucial. The Spectrum Level is defined as the root mean square (rms) of the signal after it has been filtered through a frequency band of width Δfr, centered on the frequency fr. For rotor noise analysis, it is essential to use this definition of Spectrum Level, as it focuses on harmonic signals.

This type of analysis plays a crucial role in assessing rotor noise, as it helps differentiate between tonal and broadband noise. Consequently, it enables the identification of the primary mechanisms responsible for the noise. The primary sources of tone noise depend on the rotor tip speed, and the flow conditions in which the rotor is operating. Our understanding of rotor noise is based on the

Ffowcs-Williams and Hawkings equation given by Glegg and Devenport, 2017

$$\rho'(x,t)c_\infty^2 = \frac{\partial^2}{\partial x_i \partial x_j} \int_{V_0} \left[\frac{T_{ij}}{4\pi r |1 - M_r|} \right]_{\tau = \tau^*} dV(z) \tag{1.1}$$

$$- \frac{\partial}{\partial x_i} \int_{S_0} \left[\frac{p_{ij} n_j}{4\pi r |1 - M_r|} \right]_{\tau = \tau^*} dS(z) + \tag{1.2}$$

$$\frac{\partial}{\partial t} \int_{S_0} \left[\frac{\rho_\infty n_j V_j}{4\pi r |1 - M_r|} \right]_{\tau = \tau^*} dS(z) \tag{1.3}$$

At low speeds, the loading noise, represented by the second term in Eq. , typically serves as the primary source of sound. This suggests that the radiated noise originates from the steady and unsteady pressure acting on the blade surface. Numerous factors can affect the blade loading and, consequently, the resulting noise.

The sound generated by variations in steady loading applies to all propellers but is generally a weaker noise source compared to unsteady loading. Most propellers operate in nonuniform, distorted inflow conditions, causing their angle of attack to change continuously during rotation. Gradual changes in the angle of attack are typically less significant; however, when a blade encounters a sudden velocity deficit in the flow, the resulting rapid change in angle of attack leads to a sharp variation in blade loading. In the far-field approximation, it is demonstrated that sound is produced by the time-dependent variation in loading. Therefore, a blade encountering a velocity deficit that triggers a sudden loading change can act as a highly effective noise source.

In addition to unsteady loading noise, the third term in Eq. (1.3) indicates a contribution from the motion of the blade surface, known as thickness noise. This type of noise becomes significant only when the tip speeds reach Mach numbers greater than 0.7. The mechanism for this source is the time varying displacement of fluid by the blade volume as it rotates. To the fixed observer in the acoustic far field it is as if the blade volume changes as it rotates, and this apparent variation in volume causes a sound wave in the far field. The simplest way to reduce thickness noise is to reduce the blade volume near the blade tip.

When the blade tip speed reaches transonic or supersonic levels, shock discontinuities may form on the blade surface and in the surrounding fluid near the blade tips. This phenomenon is categorized as quadrupole noise, as it originates within the fluid volume rather than on the blade surface. From the observer's viewpoint, these shocks appear to change with the blade's rotation, thereby generating sound. In some rotor designs, this noise generation mechanism can be as significant as thickness noise. Generally, thinner blades produce weaker shocks: blade tip thinning is an effective strategy for reducing noise in transonic and supersonic rotor operations.
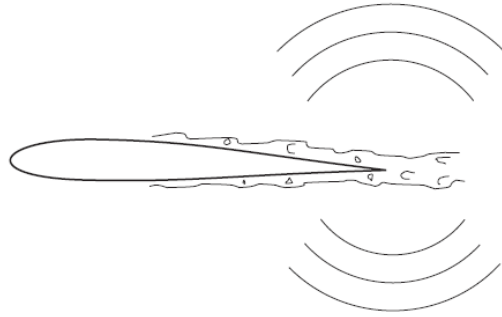
Figure 1.1: Trailing-edge noise from the blade boundary layer interacting with the trailing edge of a blade from Glegg and Devenport, 2017

Broadband rotor noise is caused by random variations in blade loading resulting from the interaction of the blades with turbulence. The turbulence is often generated upstream of the propeller and ingested into the rotor, but it can also be self-generated in the blade boundary layer or at the blade tips.

On a smooth surface, pressure fluctuations associated with turbulence are convected at a speed that is less than (or equal to) the local flow speed, and in most cases of interest this is subsonic. The far-field sound can therefore only be caused by the interaction of the turbulence with an edge, or a discontinuity on the surface, both of which scatter wave energy into acoustic waves.

The two most important examples are leading edge noise, where turbulent gust impinges on the leading edge of a blade, and trailing edge noise in which turbulent boundary layer pressure fluctuations are convected downstream across the blade trailing edge.

In summary, the turbulence in the blade boundary layer does not generate much sound by itself, but when it passes the blade trailing edge the local boundary conditions change rapidly, and significant sound generation can occur. This process is illustrated in Figure (1.1). This is trailing edge noise and is often considered as the most important mechanism of broadband noise generation in fans and propellers. Chapter 16 of the book Glegg and Devenport, 2017 outlines other key mechanisms of noise generation in propellers and rotors. In this discussion, we've highlighted some of the major sources of propeller and rotor noise. It's clear that multiple mechanisms are at play, and their significance can vary depending on the specific application or operating conditions. In some cases, several mechanisms might be equally influential, while in others, a single one might dominate.

1.2.2 Duct Acoustics

In many applications aeroacoustic sources occur in ducted environments, such as drones or unmanned aerial vehicles. The duct has a large impact on both the flow through the engine and the acoustic source efficiency, it is therefore of our interest to observe how the noise propagates within the duct.

Hard-walled Cylindrical Ducts, No Mean Flow

To obtain expressions for the acoustic pressure both inside and radiated from semi-infinite ducts first consider the harmonic solution to the sound field inside an infinite duct. We consider an infinite cylindrical duct of radius a with no mean flow. A sketch of the ducted source and associated coordinates is shown in Figure (1.2).
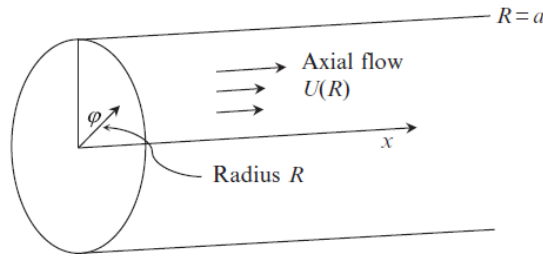
Figure 1.2: Sketch of source distribution inside a semi-infinite duct and associated coordinates (Baddour et al., 2024)

It is assumed a pressure field p is harmonic in time t, at a single frequency ω of the form,

$$p(X,t) = p(X,\omega)e^{i\omega t} \tag{1.4}$$

The pressure field inside an infinite, hard-walled, cylindrical duct, in cylindrical polar coordinates can be found from solution of the Helmholtz equation,

$$\frac{\partial^2 p}{\partial^2 r} + \frac{1}{r}\frac{\partial p}{\partial r} + \frac{1}{r^2}\frac{\partial^2 p}{\partial^2 \theta} + \frac{\partial^2 p}{\partial^2 z} + k^2 p = 0 \tag{1.5}$$

where k is the acoustic wavenumber, which for medium speed of sound c, is computed $k = \omega/c$. Furthermore, the pressure must satisfy the hard-walled boundary condition at the wall of the duct $r = a$, of the form,

$$\left(\frac{\partial p}{\partial r}\right)_{r=a} = 0 \tag{1.6}$$

Using the method of separation of variables, the acoustic pressure field inside the duct can be constructed from a modal sum of the form,

$$p(r, \theta, z, \omega) = \sum_{m=-\infty}^{\infty} \sum_{n=1}^{\infty} p_{mn}(r, \theta, z, \omega) \tag{1.7}$$

where each modal term has azimuthal order m and a radial order n, of the form

$$p_{mn}(r, \theta, z, \omega) = a_{mn}(\omega)\Psi_{mn}(r, \theta)Z(z) \tag{1.8}$$

where $\Psi_{mn}(r, \theta)$ is the normalised mode shape function and $a_{mn}(\omega)$ is the modal pressure amplitude. Substituting Eq. 1.8 into Eq. 1.5 and solving for the axial z component reveals,

$$Z(z) = e^{-ik_{z,mn}z} \tag{1.9}$$

where $k_{z,mn}$ is the axial wavenumber. Similarly, solving for the azimuthal θ dependence is of the form,

$$\Psi_{mn}(r, \theta) = \psi_{mn}(r)e^{-im\theta} \tag{1.10}$$

Finally, to obtain the radial r variation, the equations are substituted into Eq. 1.5 to give,

$$\frac{\partial^2}{\partial^2 r}\psi_{mn}(r) + \frac{1}{r}\frac{\partial}{\partial r}\psi_{mn}(r) + \left(k^2 - k_{z,mn}^2 - \frac{m^2}{r^2}\right)\psi_{mn}(r) = 0 \tag{1.11}$$

This is Bessel's equation which has the well-known solution

$$\psi_{mn}(r) = AJ_m(\kappa R) + BY_m(\kappa R)$$

where $J_m(\kappa R)$ and $Y_m(\kappa R)$ are Bessel functions of the first and second kind of order m and are illustrated in Figure (1.3). We see that the Bessel function of the first kind is finite for all values of κR and is zero at $\kappa R = 0$ for all m orders, except for $m = 0$. In contrast, the Bessel functions of the second kind are infinite at $\kappa R = 0$ for all orders. Both functions are oscillatory for large values of κR and decay to zero as $(\kappa R)^{-1/2}$ for large arguments.
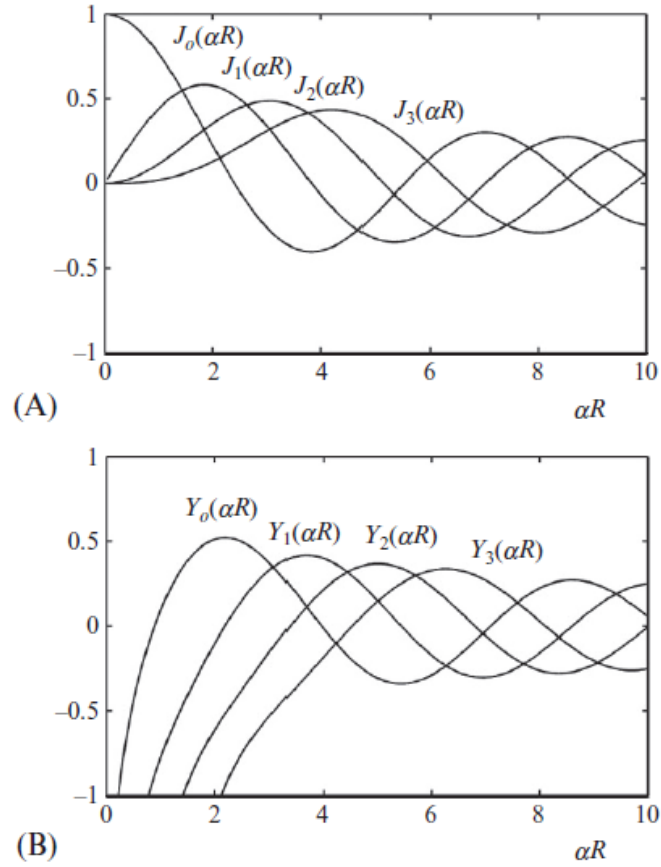
Figure 1.3: Examples of Bessel functions (A) of the first kind $J_m(\kappa R)$ and (B) of the second kind $Y_m(\kappa R)$. (Glegg and Devenport, 2017)

For the special case when the duct has no center body the sound field must remain finite at $R = 0$, and this eliminates $Y_m(\kappa r)$ as a possible solution. The sound field in the duct then only depends on $J_m(\kappa R)$. However, the solution must also match the non-penetration boundary condition on the outer duct wall, and so we require that the derivative of $J_m(\kappa R)$ with respect to R is zero at the wall where $R = a$. This is only possible for values of κ for which

$$\left(\frac{\partial J_m(\kappa R)}{\partial R} \right)_{R=a} = 0$$

There will be an infinite number of values of κ that meet this condition; these solutions are defined as κ_{mn}. The solution of 1.11 is

$$\psi_{mn}(r) = \frac{J_m(\kappa_{mn} r)}{N_m n} \tag{1.12}$$

14

where N_mn is the normalization factor, J_m is the Bessel function of the first kind of order m and κ_{mn} is the radial wavenumber, obtained by applying the hard-walled boundary condition. The relationship between the radial, axial and acoustic wavenumbers, known as the Dispersion relationship, is of the form,

$$k_{z,mn}^2 - \kappa_{mn}^2 = k^2 \tag{1.13}$$

From the dispersion equation we can identify the range of propagating modes This result delineates the range of propagating modes $k > \kappa_{mn}$ (for which $k_{z,mn}$ is purely real) and non-propagating cut-off modes $k < \kappa_{mn}$ (for which $k_{z,mn}$ is purely imaginary). Applying these conditions to Eq. 1.9 identifies that cut-off modes exhibit evanescent decay along the duct axis, where cut-on exhibit a phase change. For low frequencies all modes are cut-off except for the plane wave. We can consider a plane wave approximation (i.e. considering only the first mode) if we are far enough away from any sources, changes in boundary condition, or other scattering objects, for the generated evanescent modes to become negligible. In general we say that a mode propagates or decays exponentially depending on the frequency being lower or higher than the cut-off or resonance frequency

$$f_{co} = \frac{j'_{mn} c}{2\pi a} \tag{1.14}$$
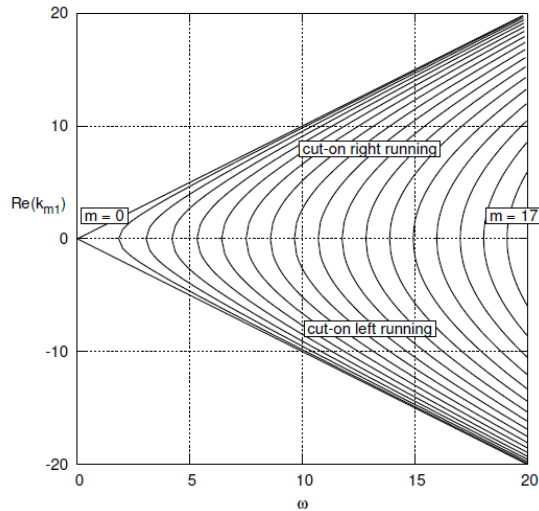
Figure 1.4: Real part of the 1st radial cut-on modes, as a function of Helmholtz number ω (Rienstra, n.d.)

In Figure (1.4) we see the first radial modes as a function of ω, and we can

15

appreciate that each m-modes are cut-on only above a certain frequency.

$$\psi_{mn}(r) = \frac{J_m(\kappa_{mn}r)}{\sqrt{\left(1 - \frac{m^2}{\kappa_{mn}^2 a^2}\right) J_m(\kappa_{mn}a)}} \tag{1.15}$$

The mode shape function represents the spacial pressure distribution inside a duct. Figure(1.5) shows the first few modes of varying m and n with the lines of zero pressure shown as black lines.
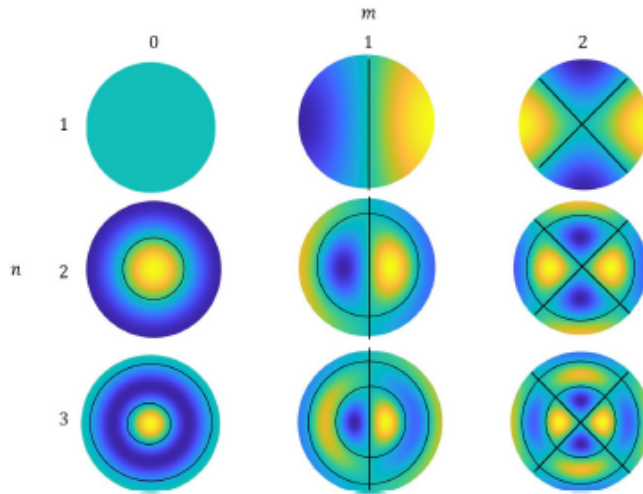
Figure 1.5: Duct mode shapes. (Baddour et al., 2024)

Hard-walled Cylindrical Ducts with Mean Flow

We now present a general formulation of the acoustic problem of sound propagation in a infinite cylindrical duct with mean flow. For simplicity, it is assumed that the mean flow is uniform in the axial direction and that there are no vortical or turbulent perturbations introduced upstream of the region of interest. In these conditions the dispertion equation changes, leading to a radial and axial wavenumbers that are functions of the velocity of the flow

$$k_{z,mn} = -\frac{kM}{\beta} \pm \sqrt{\left(\frac{kM}{\beta}\right)^2 + \frac{\kappa^2}{\beta^2}} \tag{1.16}$$

$$k_{mn} = \sqrt{k^2 - \kappa_{mn}^2 \beta^2} \quad , \quad \beta = \sqrt{1 - M^2} \tag{1.17}$$

First we note that the $\pm$ sign is chosen to represent waves propagating in the positive or negative x direction when the value of the square root is real and

taken to be positive. When the argument of the square root is negative (which occurs when $\beta\kappa_{mn} > k$) then it must have a positive imaginary part to ensure that the wave decays in the direction of propagation. It follows that waves will either propagate as waves or decay with distance in either the upstream or downstream direction. The rate of decay depends on the "cutoff" ratio

$$\xi_{mn} = \frac{\beta\kappa_{mn}}{k} \tag{1.18}$$

If the cutoff ratio is large $\xi_{mn} >> 1$ then the value of μ_{mn} has a large positive or negative imaginary part, and the duct mode of order (m, n) decays rapidly with distance along the duct. On the other hand, when the cutoff ratio is very small then the value of k_{mn} is real, and the duct mode of order (m, n) propagates along the duct without attenuation.

The decay of cutoff modes is an important feature of duct acoustics because it limits the number of acoustic modes that will propagate from a source to a duct exit, where they can radiate to the acoustic far field. If the source is a large distance fromt he duct exit then the cutoff modes play no role in the far-field radiation, but if the source is close to the duct exit then cutoff modes cannot be neglected. The rate of decay of a cutoff mode depends on

$$e^{-(k|x|/\beta^2)\sqrt{\xi_{mn}^2-1}} \tag{1.19}$$

where $|x|$ is the distance from the source. When $\xi_{mn} >> 1$ the amplitude of the mode decays to zero over a distance that is a fraction of an acoustic wavelength. However, when the mode is close to cut off then the decay is relatively slow. This is important because the fan design can be tailored so that the acoustic modes are cutoff, and this can result in significant far-field noise reductions.

Due to the mean flow, the axial modal wave numbers are shifted to the left $(M > 0)$, while the (dimensionless) cut-off frequency is lowered from $\omega = \kappa_{mn}$ for no flow to $\omega = \beta\kappa_{mn}$ with flow. Consequently, with flow more modes are possibly cut-on with respect to the case with no flow.
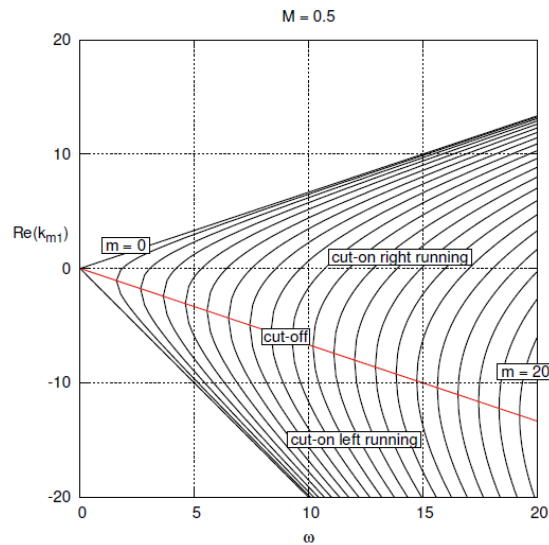
Figure 1.6: Real part of the 1st radial cut-on modes, as a function of Helmholtz number ω (Rienstra, n.d.)

1.2.3 Ducted Rotor Noise

The main difference between a ducted fan and an open rotor is the presence of the duct, which shapes how acoustic sources interact with the far field. In a ducted fan, sound excites specific duct modes, determined by the boundary conditions at the duct walls, which strongly influence how noise propagates to the outside.

In the 1970s high bypass ratio turbofan engines were introduced, enabling a large increase in engine diameter so the same thrust could be achieved with a lower jet speed. The jet noise component of the sound was significantly reduced by the lower jet exit velocity and other sources such as fan noise became significant contributors to the overall noise level.

Initially the far field sound, especially at low thrust conditions, was dominated by tone noise from the engine fan. However, as the fan diameter is increased the broadband fan noise also increases and contributes more energy to the far field, so in very high bypass ratio turbofan engines the tone noise and broadband noise are of equal importance.
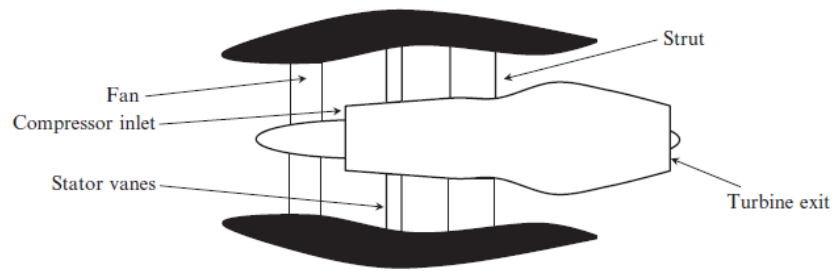
Figure 1.7: Schematic of a high bypass-ratio turbofan engine(Glegg and Devenport, 2017)

Ducted fans and open rotors share some noise generation mechanisms but differ due to the effects of the duct. The duct allows sound to propagate in specific modes, depending on the frequency, and creates opportunities for noise reduction using sound-absorbing materials. This design can attenuate noise before it reaches the duct exit. However, in short ducts, non-propagating modes may still escape and contribute to the far field.

Key noise sources for ducted fans include unsteady loading noise and trailing edge noise. Thickness noise is generally less significant because, at subsonic tip speeds, the relevant duct modes are cut off. However, at supersonic tip speeds, these modes propagate and contribute to radiation.

Unsteady loading noise arises from non-uniform inflow conditions, often shaped by the duct inlet design and upstream obstructions. Small turbulent eddies in the atmosphere can stretch and deform as they enter the duct, creating a spiral shape that interacts with rotating blades. This interaction can produce distinctive fan tones, known as haystacking, which are particularly noticeable during ground operations due to atmospheric turbulence. In flight, this effect diminishes because the relative motion between the engine and the atmosphere reduces the inflow's distortion.
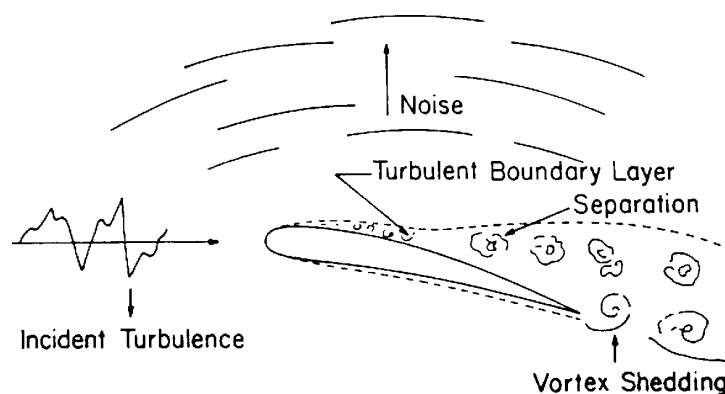
Figure 1.8: Turbulent impinging flow

19

During flight, the dominant noise source shifts to the interaction between fan blade wakes and downstream stator vanes. This interaction generates both tonal and broadband noise, influenced by the swirling flow in the duct. The broadband noise depends heavily on the intensity and scale of turbulence at the leading edge of the stator vanes.

Broadband self-noise from the fan also contributes to the far-field spectrum, especially at high frequencies. This noise results from interactions with the duct wall boundary layer, tip flows between the fan blade and duct wall, and trailing edge noise. For large fans, trailing edge noise is the most significant of these mechanisms, while turbulence in the duct wall boundary layer can be a notable contributor in smaller or model-scale fans.

1.3 Purpose of this thesis

The objective of this thesis is to quantify and understand the effect of duct length on the generation and radiation of noise both inside and outside the duct. Two different ducts, differing in length but with identical intake geometry, are tested and compared using both near-field and far-field measurements. On the setup previously used by Palleja-Cabre et al., 2024, near-field measurements were added inside the duct, enabling simultaneous acquisition of near- and far-field noise data.

To better understand the impact of duct length, velocity field measurements along the duct wall were also performed, aiming to characterize the aerodynamics of the system and evaluate its influence on noise generation. Due to the specific geometry of the lip intake, a strong boundary layer separation occurs near the leading edge of the duct, which subsequently interacts with the blade's rotation. Under hover conditions, this flow separation produces a highly turbulent and inhomogeneous flow near the wall, which impacts the noise source. The interaction between the separated flow and the propeller, along with the subsequent scattering of vortical structures at the duct's trailing edge, is hypothesized to be a significant noise source in this system, contributing to both tonal and broadband noise. Through the microphones, we reconstructed the distribution of the sound level inside the duct, both along the axial direction and the azimuthal opening, identifying the frequency range of greatest interest. Finally, building on the trend of passive acoustic treatments, the effect of a metal foam liner, flush mounted on top of the propellers plane, was investigated. This thesis is is structured as follows:

- **Chapter 2** : Explanation of the experimental setups adopted in this project, with a brief explanation of the effect of intake geometry.

- **Chapter 3** : Brief explanation of the setup used to make Hot-Wire Anemometry measurements and presentation of the flow velocity results obtained.

- **Chapter 4** : The radiation of noise in the far field and the propagation of noise inside the duct are presented, aiming to identify and explain the differences observed between the two ducts.

- **Chapter 5** : The effect of introducing a metal foam liner inside the duct is analyzed. The results are compared with the baseline configuration of the long hard-walled duct, aiming to identify the strengths of this acoustic treatment, both in terms of propagation and attenuation inside and in the outside the duct .

- **Chapter 6** : Summarises the conclusions and future works related to the project.

21

Chapter 2

Experimental Set-Up

2.1 Anechoic Chamber Set-up and Propeller Design

The experiments were carried out at the Institute of Sound and Vibration Research's recently refurbished anechoic chamber, of dimensions $6.7m \times 6.7m \times 4.9m$. The chamber's walls are acoustically treated with open-cell polyurethane wedges whose cut-off frequency is $70Hz$. The rotor and the duct used in this research are the same one used by Palleja-Cabre et al., 2024 in their study. The experimental investigation is performed using a modular shroud rig containing a single propeller.

The rotor is powered by a U7-V2.0 KV420 Brushless T-motor mounted on a MINI45 ATI 6-axis loadcell. The propeller, the motor and the loadcell are held on the axis of the shroud by vertical rod located downstream of the propeller plane. The electronic speed controller used in conjunction with the motor is a Master Mezon 135 opto unit. To measure the rotational speed of the propeller (Rotations Per Minute, RPM) an ICP Laser Tachometer sensor is used. The propeller used in this experimental set-up is a 2-bladed MEJZLIK with a diameter of 16 $inches$ ($40, 64 \, [cm]$). Near-field and far-field noise measurements were taken by using quarter-inch GRAS 40PL-10 CCP microphones.
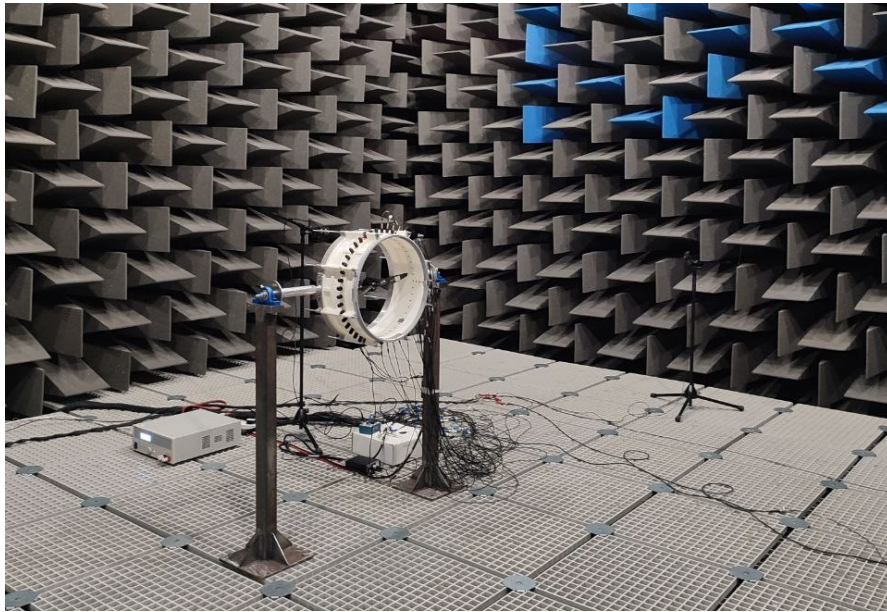
Figure 2.1: Experimental rig at the Institute of Sound and Vibration Research's anechoic chamber
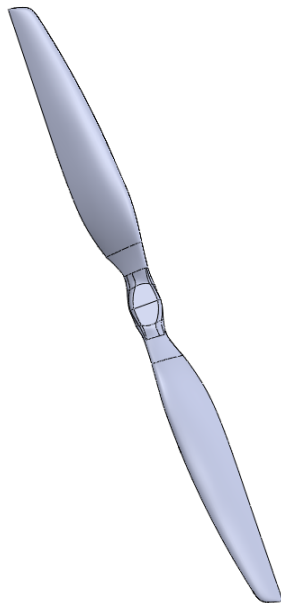
Figure 2.2: CAD view of the 2-bladed MEJZLIK 16 *inches* propeller
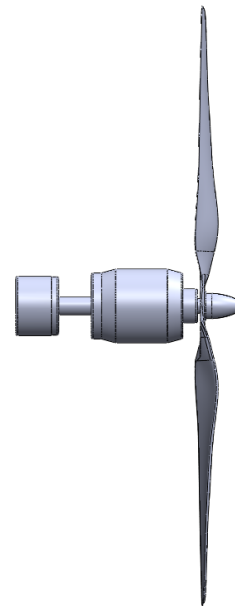
Figure 2.3: CAD view of the airframe

2.2   Shrouded Propeller Rig

The experimental investigation is performed using a 3D printed modular shroud rig. Each module that composes the duct is 1/3 of the circumference and adds $5cm$ length to the duct. The modules are printed in such a way that they can be interlocked with each other, in order to minimize openings along the inner wall of the duct. Studs mounted outside the duct are used to keep each module in place, close eventual gaps and maintain the duct axisymmetric. This set-up allows us to create different shroud rigs: we can play with the length of the duct, it's possible to install acoustic treatments in the casing, such as SDOF liners or more complex metal foam liners, and gives us the chance to mount different intake geometries. This specific setup not only allows us to vary several problem parameters, duct length, wall type (hard-wall or porous materials), and intake geometry, but it is also extremely useful in this initial project phase to obtain various types of experimental data. The following is a list of various elements/modules that can be mounted on the duct in order to acquire different data:

(a) Circumferential module used to install microphones inside the duct. The module allows us to study the acoustic field created inside the duct,taking *near-field NF* noise measurements. This module increases the duct's length by $20cm$.

(b) Axial module used to position 3 microphones along the axis of the duct, at the same azimuthal angle.

(c) Module used to make Hot-Wire measurements inside the duct. This set-up element has a single hole through which the HW and probe holder can pass across.

The shroud is installed onto two legs and each of them is fixed to the gridded floor of the anechoic chamber Figure(2.1). In this project we analyzed three different set-ups: two of them are used to evaluate and compare the results for short and long duct configuration, while the third one is used to investigate the impact of passive acoustic treatments.
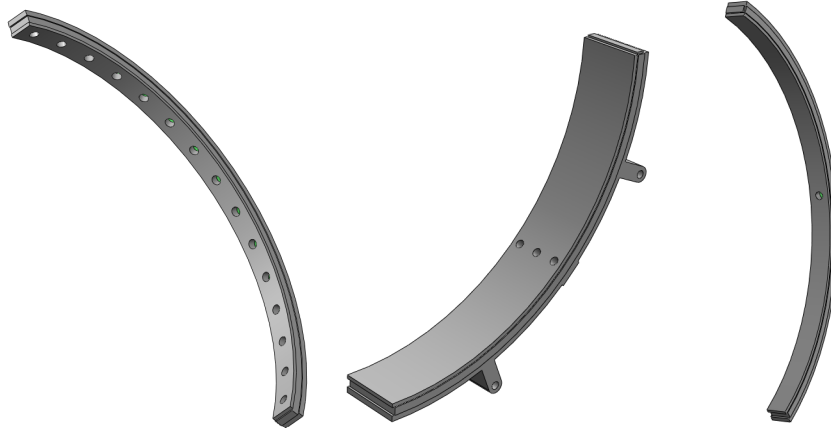
Figure 2.4: Modules used to take different acoustic and flow measurements

2.2.1 Intake Geometries

The effect of different intake geometries on sound propagation was already explored by Palleja-Cabre et al., 2024. A part of their project was dedicated to investigate the impact of two different intake geometries on noise propagation:

- Bellmouth intake : the geometry of this intake is designed to aerodynamically optimize the flow entering the duct. As the name suggests, a bellmouth inlet duct is a type of convergent inlet used to direct air inward. The geometry is manufactured to lead-in the airflow, created by the blade rotation, seeking to minimize the aerodynamic losses due to boundary layer separation.

- Lip or unflanged intake : the lip intake geometry is not designed to improve aerodynamic performance; as will be shown in the following chapters, the sudden leading edge leads to the generation of new noise sources.

Some of the conclusions in Palleja-Cabre et al., 2024 have shown that the intake geometry has a significant impact on the generation of noise, which is likely mainly caused by different inflow conditions onto the propeller. Among these are enhanced propeller-boundary layer/turbulence interaction noise and inflow distortion. To minimize the noise of shrouded rotor system, careful aerodynamic intake design is essential.

In this thesis, we carried out the evaluation of another relevant variable of the system, the effect of duct length on the propagation of noise. The precedent studies highlight that the configuration with the unflanged intake is the least favourable, without considering any acoustic treatment (OTR liners), providing an increase of broadband noise of almost $20dB$ with respect to the configuration with the bellmouth intake. The intake geometry for our experiments was chosen
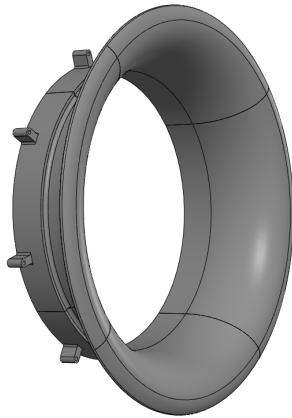
Figure 2.5: CAD view of the bellmouth intake

Figure 2.6: CAD view of the lip/un-flanged intake

based on the criterion of system simplicity. The experiments that were taken in this work are designed to enable future comparison with numerical data. To simplify the real-world system configuration, which will need to be reproduced for numerical calculations, a lip intake was chosen.

2.3 Configurations Analyzed

2.3.1 Short Duct

The short duct configuration has a total length of $180mm$, which includes a $10mm$ unflanged intake and a $20mm$ circumferential module for collecting acoustic data inside the duct, leading to an actual length of $150mm$ of hard-walled duct. Near-field noise measurements were taken by 25 microphones

- 3 microphones located in the axial module

- 22 microphones on the shroud rig, the circumferential microphones. Due to the system's symmetry, we placed the microphones on half of the duct's circumference.

Figure (2.7) shows a sketch representing the two duct length configuration and the position of the near-field microphones. The pink microphones represent the circumferential module, where we placed 25 microphones. The blue dots indicate 3 axial microphones, which are positioned at the same azimuthal position, but different axial position. As we can see from the Figure, we aligned the the shroud

26
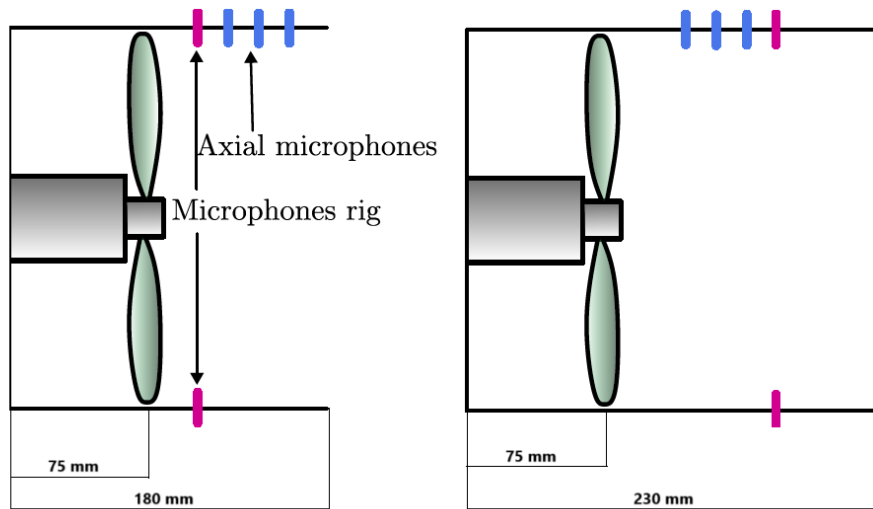
Figure 2.7: Sketch of the short and long duct configurations and location onf in-duct microphones

rig with the axial microphones, so that we could have 4 different axial measurements points. Furthermore, far-field noise measurements are obtained by using 3 microphones positioned at $2,5m$ radius form the propeller rig.
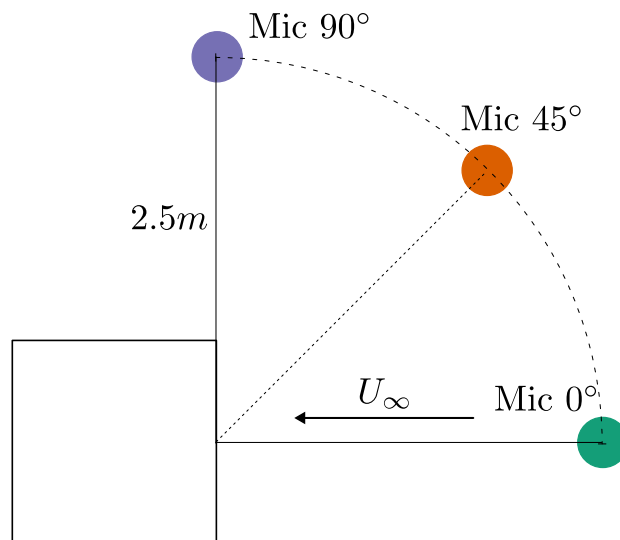
Figure 2.8: Sketch of the location of far-field microphones

With this shroud set-up we also wanted to see the changes in noise propagation and radiation created by moving upstream, towards the open-end of the duct, the

propeller plane. We also took advantage of the flexibility of this modular shroud test rig to have noise measurement from different axial position inside the duct. This lead us to 4 different configuration for the short duct set-up:

1. In this configuration all the microphones are located upstream of the propeller plane.

2. We positioned the propeller plane upstream, keeping the microphones in the same location. Consequently, the circumferential module is on top of the propeller plane.

3. The propeller plane is located in the same position as for 1. configuration, but we changed the site of the microphones. In this particular scenario some of the microphones are downstream the rotor, while others are upstream of it.

4. The microphones are left in the same position of 3., while the propeller plane is moved upstream towards the open-end of the duct, having the microphones downstream the propeller plane.

2.3.2   Long duct

The long duct configuration has a total length of $220mm$, created by adding $50mm$ length after the 3 axial microphones module from configuration 1..
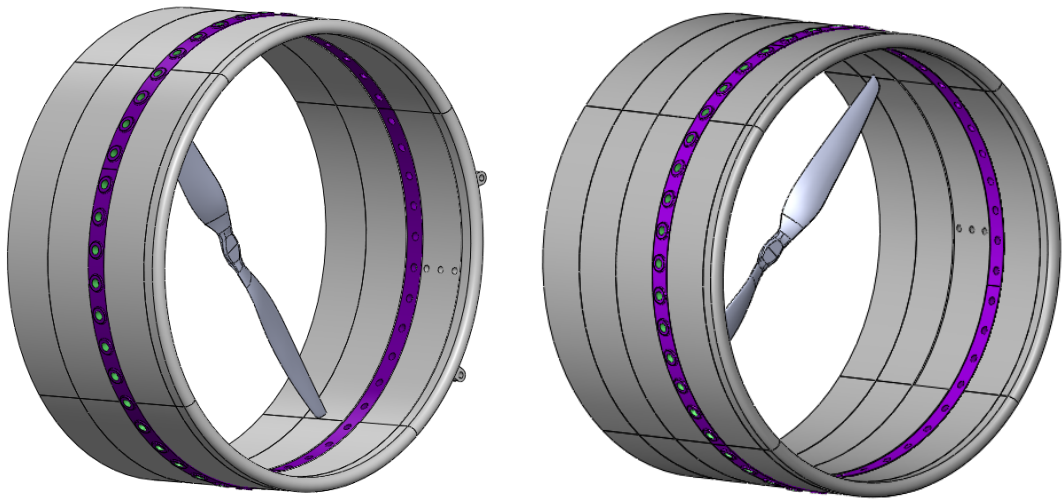
Figure 2.9: CAD view of the short setup   Figure 2.10: CAD view of the long setup

2.3.3   Long lined duct

One of the goals of this project is to advance the understanding and application of metamaterials, while addressing the critical issue of noise reduction. To do that we installed an Over-Tip-Rotor (OTR) grooved metal foam liner in our modular system Figure (2.11).
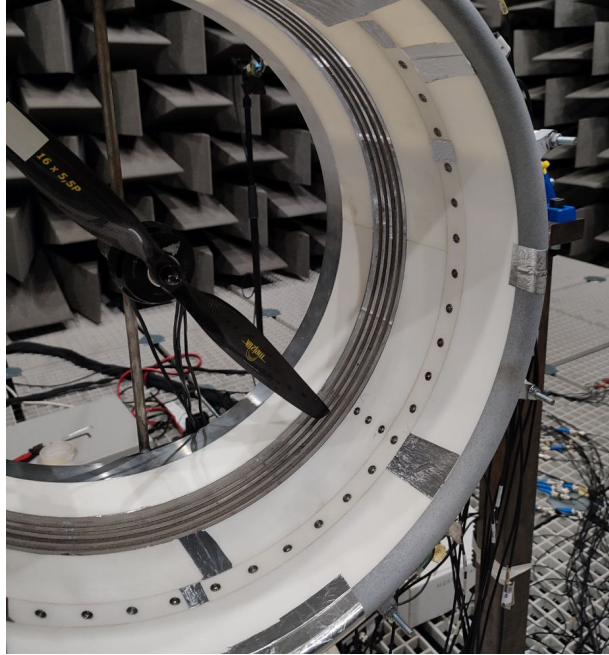
Figure 2.11: Picture of the long lined setup

The passive acoustic treatment is a grooved liner in which the annular grooves are filled with a metal foam of Nickel Chromium Alloy flush with the shroud inner wall. A summary of the liner design parameters is shown in Table (2.1), where POA is the Percentage Open Area, h is the cavity depth and σ is the porosity of the metal foam.

Table 2.1: Liner design parameters

Liner	Type	$h\,[mm]$	$POA[\%]$	$\sigma\,[\%]$
Grooved	semi-locally reacting	17.5	44	90

The liner is locally reacting in the axial direction and non-locally reacting in the azimuthal direction. Note that this POA only accounts for the grooved area relative to the total liner area and not the open area of the metal foam within the grooves.

Chapter 3

Hot-Wire measurements

3.1   Experimental Set-Up

In order to have an idea of the flow distribution and the velocity orders of magnitude we performed velocity measurements with the use of Hot-Wire Anemometry (Dantec Multichannel CTA). The setups chosen for these measurements are the short and long hard-walled duct configurations.
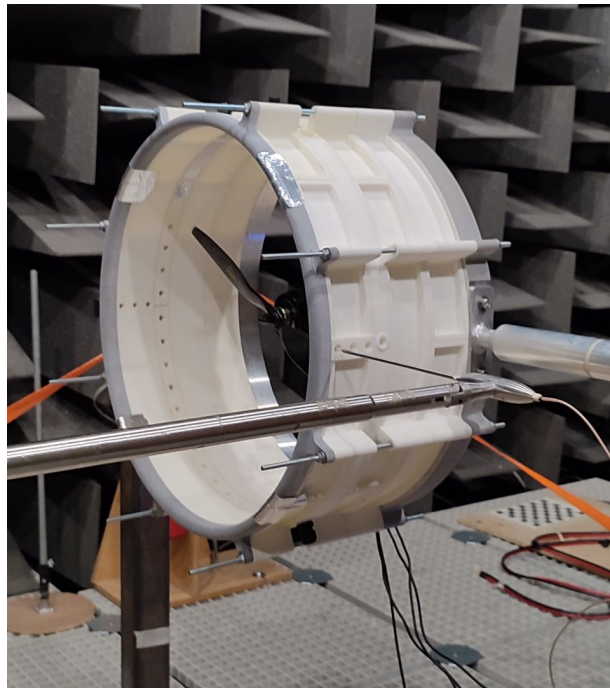
Figure 3.1: Picture of the short setup for Hot-Wire measurements

The target of these measurements is to enable us to understand the evolution of the flow impinging onto the propeller. To achieve this, we took hot-wire measurements at two positions along the duct axis for both the configurations. As depicted in Figure (3.1), velocity measurements were taken near the open end of the duct and at another point further inward, towards the propeller plane.
The shroud casing is instrumented to allow traversing a single wire probe in the radial direction r. The circumferential module for microphone positioning along the duct diameter was replaced with a module designed for hot-wire measurements Figure(2.4). Measurements along the radial direction were taken from the inner surface of the duct up to $r = 105mm$, covering 50% of the inner radius of the duct ($R_0 = 205mm$). To reconstruct the boundary layer, 60 measurement points were used between $r/R_0 = 0.5$ and $r/R_0 = 1$.

Acquisition parameters were set with a sampling frequency of $40kHz$ and 600000 samples acquired, for a duration of 15 s. The probe is driven by a constant temperature bridge and the hot wire is positioned to measure the velocity in the direction of the fluid flow *streamwise*. The probe was mounted on a remotely controlled 3D traversing system. Measurements are obtained in two location upstream of the propeller plane (in the axial direction), table (3.1)

Table 3.1: Position of the HW probe relative to the propeller plane

	Short Duct	Long Duct
Position 1	88[mm]	138[mm]
Position 2	52[mm]	102[mm]

3.2 Mean Flow Results

The mean flow velocity profiles captured in Position 1 upstream of the propeller, for both duct lengths, are shown in Figure (3.2) and Figure (3.3) respectively.

Due to the lip intake, we see a large region of velocity deficit, corresponding to high turbulence intensity, centred at around 90% of the radius, likely associated with flow separation at the lip.
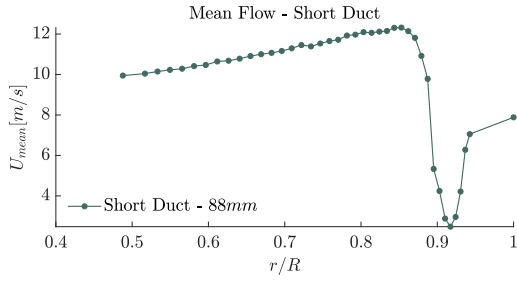
Figure 3.2: Flow velocity profiles measured $88mm$ upstream of the propeller plane in the short duct
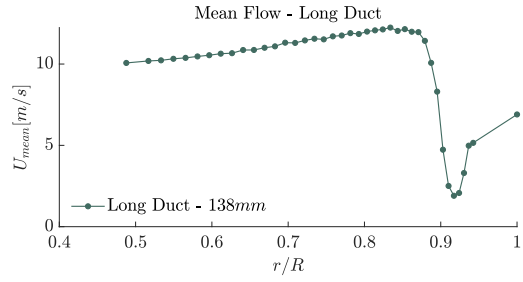
Figure 3.3: Flow velocity profiles measured $138mm$ upstream of the propeller plane in the long duct

To compare the two setups Figure (3.4) depicts the normalized mean flow profiles of the two ducts. We can appreciate how the $U_{norm} = U/U_{max}$ are very similar in the two configurations, reaching for the maximum value together at the same radial position. Although both measurements are taken at the same distance from the leading edge of the duct, we observe that different values are reached at the wall. However, this difference is not well captured due to the limited number of measurement points near the wall. We can hypothesize, though, that this difference is caused by possible disturbances in the path of the wall flow (such as the presence of gaps or uneven duct components).
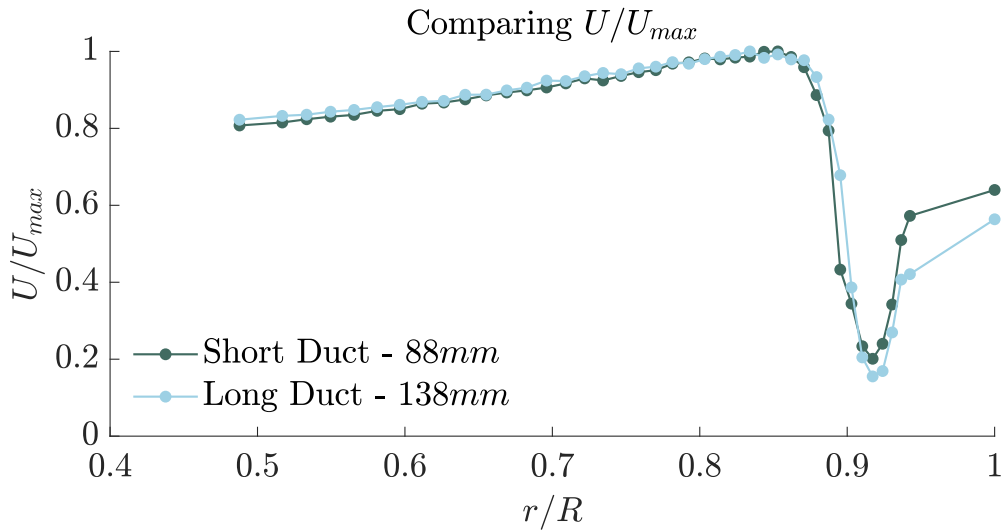
Figure 3.4: Mean Flow velocity profiles

We now focus on the characteristics of the unsteady flow upstream of the propeller to explain their influence on the generation of propeller noise. The PSD of the velocity contours are shown in Figure (3.5) for the short and long ducts respectively. This image represents the Power Spectral Density (PSD) velocity contours of a flow field, measured using Hot-Wire Anemometry. The PSD is a statistical measure that describes the distribution of the energy of a signal across different frequencies. The PSD is plotted as a function of the non-dimensional radial position (r/R) and the non-dimensional frequency BPF, the blade passing frequency. The color contours represent the magnitude of the PSD, with the higher values shown in yellow and the lower values in blue. From the Figure, we can see how the turbulent energy is distributed as a function of frequency and radial distance from the wall. The region where, from the boundary layer Figure (3.4) we observed separation, shows high energy levels, which gradually decrease as we move away from the wall. The horizontal bands appearing at the first BPF correspond to the rotation frequency of the propeller.

It is therefore expected that the separated flow will produce significantly higher levels of tonal and broadband noise, due to periodic chopping of eddies in the incoming flow (tonal) and turbulence leading edge interaction noise (broadband). Both ducted configurations might also present an increase of tonal noise relative to the isolated propeller due to mean flow distortion, not measured in the current study.
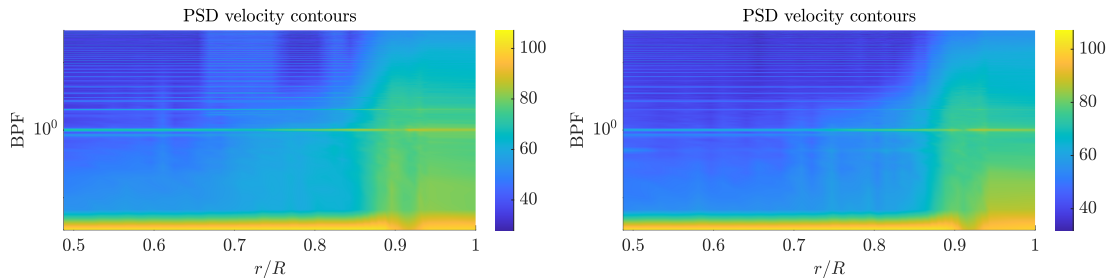
Figure 3.5: PSD velocity contours in dB plotted against normalised radius r/R_0 and Blade Passing Frequency (BPF): short duct (left), long duct (right)

3.2.1 Evolution of the Boundary Layer

By conducting hot-wire measurements at two axial locations within the duct, we were able to characterize the boundary layer evolution from the leading edge ($17mm$ from the inlet lip) towards the propeller. However, in the short duct configuration, the second measurement station was too close to the propeller ($52mm$) to

yield reliable flow data. Consequently, only data from the long duct configuration were considered.

The resulting velocity profiles are presented below, and Figure (3.8) shows a comparison of the normalized velocity profiles using U_{max}. Moving towards the propeller, the separated flow shows an increasingly larger velocity deficit, which also expands in the radial direction.
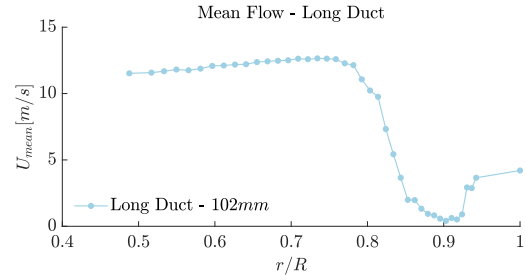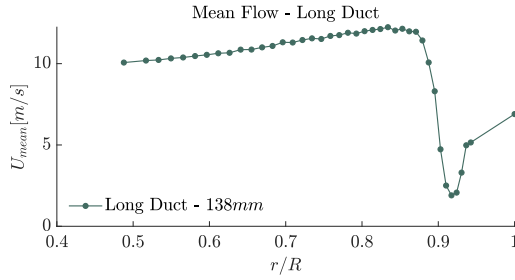
Figure 3.6: Flow velocity profiles measured $138mm$ upstream of the propeller plane

Figure 3.7: Flow velocity profiles measured $102mm$ upstream of the propeller plane
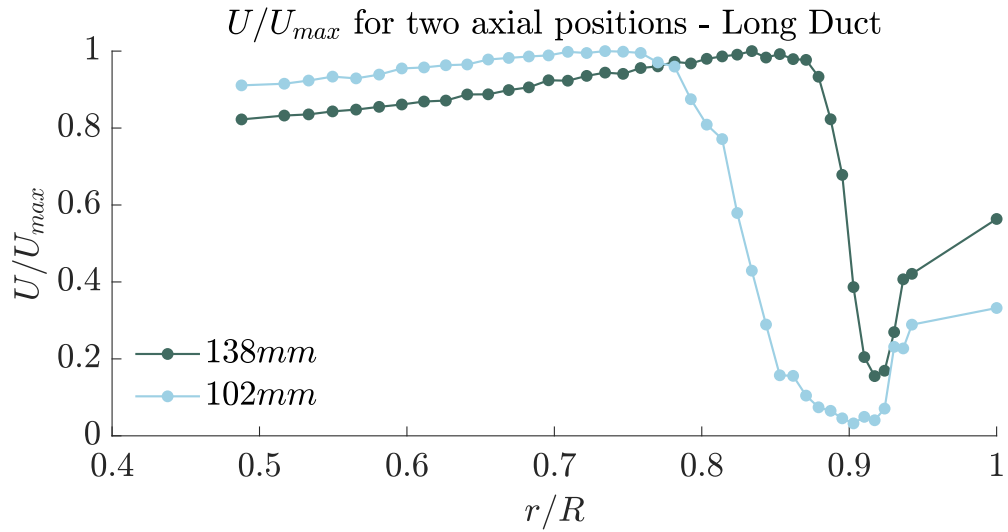
Figure 3.8: Normalized mean flow velocity profiles in the long duct setup

In terms of PSD velocity contours of the HW data, as a result, the turbulent energy level near the propeller is higher and extends also along the radial direction.

34
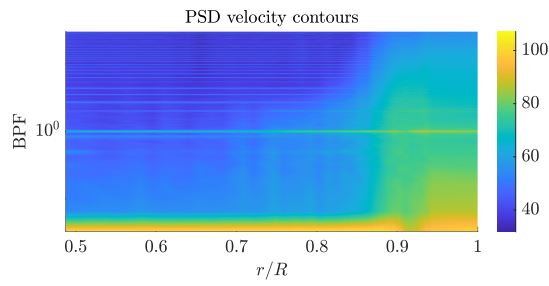
Figure 3.9: PSD of the velocity contours - 138mm
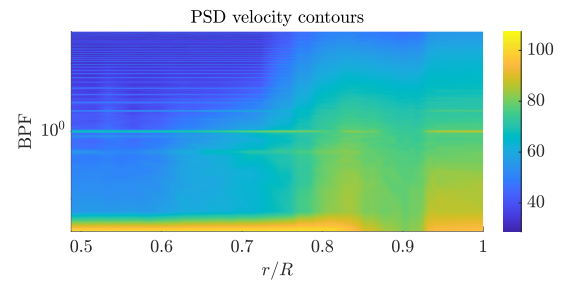
Figure 3.10: PSD of the velocity contours - 102mm

Chapter 4

Far-Field and Near-Field Noise Measurements

In this chapter, we will observe and analyze the results obtained after post-processing the data using MATLAB. The primary objective will be to assess the impact of the two duct lengths on the generation of propeller noise and its relation to the inflow characteristics. In a subsequent chapter, we will address the topic of liners and present the results obtained from the long lined configuration.

In the time domain, we observe how pressure varies with time, but this does not provide clear information about the specific frequencies involved.

Propellers generate noise primarily due to periodic events such as the passage of each blade. Each time a blade passes a microphone, it generates a pressure disturbance that has a specific frequency content related to the blade passing frequency (BPF) and its harmonics.

Aeroacoustic sources such as propellers generate also broadband noise. This noise typically consists of many different frequency components, each of which can have a different behaviour and significance in terms of how it propagates, interacts with the surrounding medium, and is perceived by listeners.

In the time domain, these periodic pressure variations manifest as a series of pulses or pressure valleys/peaks that can be difficult to analyze directly. The frequency domain, however, allows us to decompose these signals into their constituent frequencies, which makes it easier to analyze the blade passaing frequency (BPF) and its harmonics, as well as other noise components that might not be directly tied to the blade passage.

Noise are characterized by a spesific spectral content, the distribution of sound energy across different frequencies. For instance, low-frequency noise (e.g., from large, slowly rotating blades) might have different implications for the environ-

ment or for human perception than higher-frequency noise (e.g., from smaller or faster blades). By analyzing the frequency spectrum, we can identify dominant frequencies, quantify the level of tonal noise (such as harmonics of the blade passage frequency), and assess how the sound energy is distributed across the spectrum. This information is essential for understanding the sources of noise and for evaluating how to reduce or mitigate it.

In MATLAB the Fast-Fourier Transform *fft* directly computes the discrete Fourier transform *DFT* of the signal, giving the frequency spectrum of the entire signal. It provides a point-by-point transformation of the signal in the frequency domain and assumes that the signal is periodic and has no noise or other variability.

The *pwelch* function computes an estimate of the Power Spectral Density *PSD* of a signal, using a method based on periodogram averaging. The function divides the signal into overlapping segments (windows), applies a window function to each segment. Then computes the Fourier Transform of each segment, averages the results over multiple windows to reduce variance in the spectral estimate, making it more stable than a raw *fft*. It's designed to give a smoother and more reliable estimate of power versus frequency.

4.1 Comparison isolated and shrouded propeller

In our experimental campaign no noise measurements were taken of the isolated propeller. In this small section we are going to asses the effect of a hard walled duct on the noise radiation of a propeller, showing the results obtained for an isolated propeller by Palleja-Cabre et al., 2024 in their experimental investigation. In their project far-field noise measurements were obtained by using a horizontal arc array of $3m$ radius centred on the propeller rig. The array consisted of 15 quarter-inch GRAS 40PL-10 CCP microphones equally spaced between 0° to 90° from the propeller axis. The array was located upstream of the propeller rig and the measurements were carried out for a duration of $10s$ at a sampling frequency of $40kHz$. The results for this three different setups were acquired at a constant propeller thrust of $T = 10$N, adjusting accordingly the RPM values.

The Sound Power Level spectra

$$\text{PWL}(w) = 10 \, log_{10} \left(\frac{S_w(w)}{W_{ref}} \right) \tag{4.1}$$

is calculated here by integrating the Power Spectral Density *PSD* of the acoustic pressure over the microphones array, where $S_w(w)$ is the sound power spectral density and $W_{ref} = 10^{-12}W$.

The PWL noise spectra of the hard wall configuration for the two types of intake, bellmouth and unflanged, are shown in Figure (4.1). Also shown in Figure

(4.1) is the spectrum for the propeller in isolation (producing the same thrust).
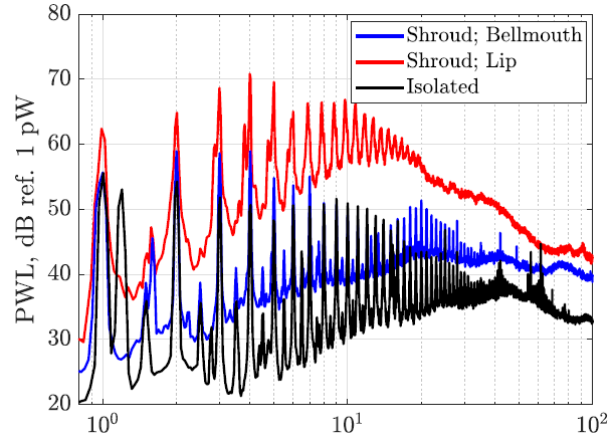
Figure 4.1: Comparison of the sound power level for an isolated and shrouded propeller with a bellmouth and lip intake

It can be observed that both ducted configurations are significantly louder than the isolated case for the same thrust conditions. This is most pronounced in the configuration with the lip intake, which shows broadband levels up to $20dB$ higher than the bellmouth counterpart, and almost $30dB$ higher than the isolated propeller.

We can observe that the increase in noise is not the only difference among the three cases considered. In the case of the duct with a lip intake, we notice a particular hump at high frequencies, a characteristic not present in the case of the duct with a bellmouth intake.

In this paper, Hot-Wire measurements were also performed to reconstruct the flow behavior at the wall of the two ducts. As already shown by our data, the duct with a lip intake generates significant boundary layer separation, characterized by high levels of turbulence intensity. Conversely, the case with a bellmouth intake does not exhibit separations Figure (4.2).
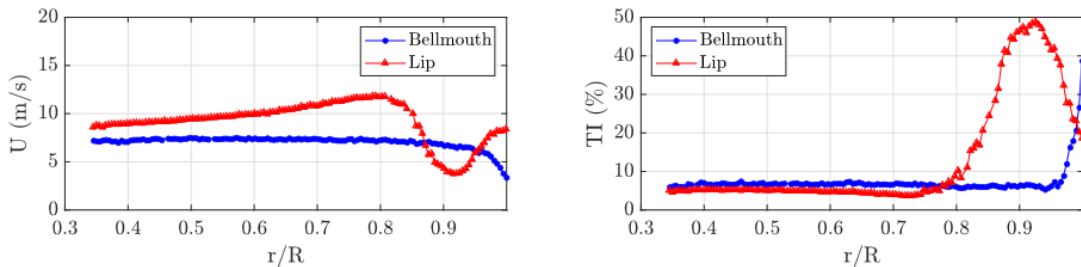
Figure 4.2: Flow velocity profiles measured 40 mm upstream of the propeller plane

It is hypothesized that this hump at high frequencies is a result of the flow distortion generated by the unflanged intake, leading to stronger scattering at the trailing edge of the duct.

4.2 Far-Field Noise from Short and Long Duct Configurations

In this section, we are going to analyze and compare the far-field acoustic radiation from the short and long duct configurations. Far-field acoustic measurements were obtained using three microphones, positioned 2.5 meters from the test rig, at $0^o, 45^o$ and 90° degrees relative to the propeller axis of rotation. With these three microphones positioned in the far field, we aim to observe how the radiated sound field changes as the duct length varies.

To better understand the difference in the spectra of the two setups, Figure (4.5) shows the SPL in the far-field measured from the short duct configuration (solid lines) and the long duct configuration (dashed lines). It is clear from Figure (4.5) that the configuration with the longer duct is the loudest in the far field. This is an unexpected result, inconsistent with the predictions made by analytical studies on noise propagation and radiation in ducts.
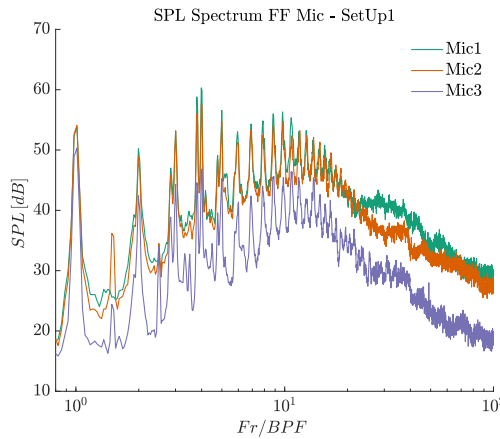
Figure 4.3: SPL Far Field short duct configuration
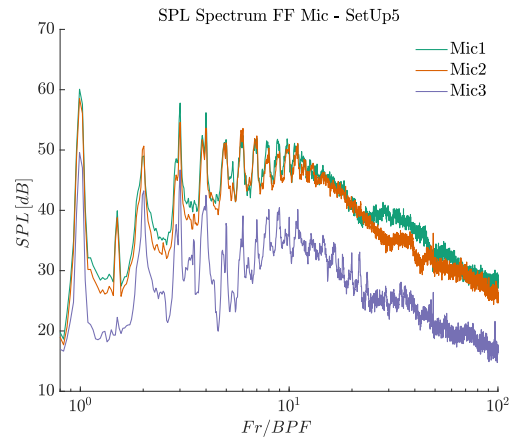
Figure 4.4: SPL Far Field long duct configuration

In order to have a clearer understanding of the differences between the two configurations we can distinguish from the far-field noise spectrum broadband noise and tonal noise (Appendix A).

39
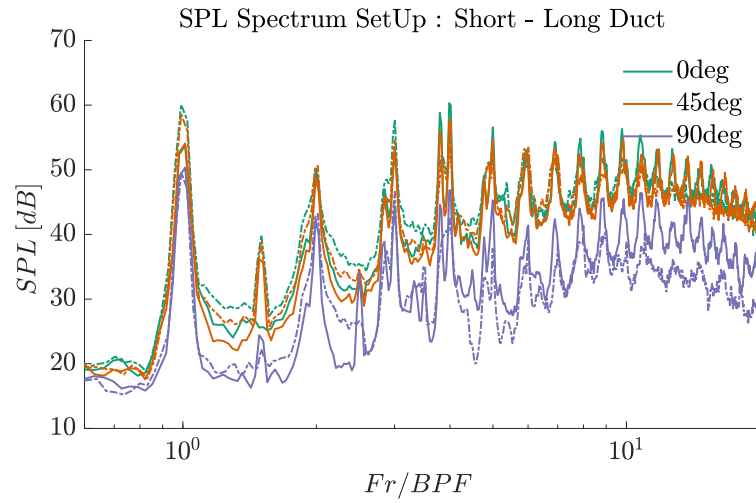
Figure 4.5: Comparison of the sound power level for short (solid lines) and long (dashed lines) shrouded setups with lip intake

Figure (4.6) shows the difference in broadband and tonal noise from the short and long configurations, for all three far-field microphones. Positive values indicate that the short configuration is more noisy, while negative values show that the longer duct has the highest sound levels.
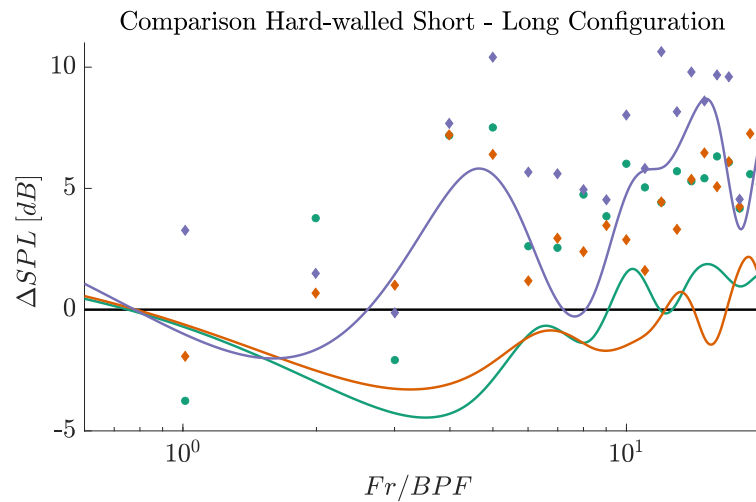
Figure 4.6: Comparison of the sound power level for short and long shrouded setups. Broadband noise difference (solid lines), tonal noise difference (points)

Microphones positioned at 0 and 45 degrees relative to the propeller axis exhibit a similar pattern: the long configuration generates higher broadband noise, with a maximum of $5dB$ in the first 10BPFs , while at higher frequencies, the difference between the two configurations oscillates around zero.

The microphone at 90 degrees shows a different pattern, but also indicates about $2dB$ higher noise levels for the long configuration at the first 2BPFs. For higher harmonics, the short configuration produces louder broadband noise levels.

Having higher broadband noise in the long configuration could tell us that this setup may generate more turbulence at the inlet of the duct, causing higher leading edge and trailing edge noise. Another mechanism generating higher broadband levels for this setup could be scattering of turbulent structures, such as blade tip vortices interacting with the boundary layer of the duct and (as for trailing edge noise) subsequent interaction of this turbulence with the edge at the open-end of the duct. Another relevant parameter that could explain the behavior of the long test rig is the axial asymmetry in the location of the propeller plane within the duct. Different studies (Simon et al., 2023), both numerical and experimental, have shown that the best noise attenuation is achieved when the propeller is centered axially in the duct, because of interference between upstream and downstream radiated waves. The study demonstrates the acoustic benefit of centering the propeller axially in the duct to maximize destructive interference between upstream and downstream radiation in hover conditions.

Regarding tonal noise, just the first harmonics show higher levels for the longer duct. Higher multiple of the blade passing frequency show that the short configuration has greater tonal noise levels. Since the first $2-3$ harmonics are mainly due to loading noise, this may be an indication that the pressure distribution on the propellers blade may be a bigger source of noise in the longer configuration, compared to the shorter one. It is worth noting that the shorter configuration shows more pronounced tone peaks, especially at higher frequencies, with respect to the longer configuration Figure (4.5). After the first 10BPFs the noise spectra of the long duct is mainly due to broadband noise.

4.3 Axial Microphones

The set-up has a total of 28 microphones, 25 of them are placed to measure the near-field noise inside the duct, while the rest of them are located at $2.5m$ from the propeller test rig to measure far-field noise. In this section, we will conduct a thorough analysis of the signals captured by the in-duct microphones, exploiting both their axial and circumferential placements. By taking advantage of the different arrangement of the microphones inside the duct, both in the axial direction and along the azimuthal angle, we aim to reconstruct the distribution of

the sound energy level near the source and study noise attenuation along the wall of the duct, seeking to highlight potential differences between the two ducts.

4.3.1 Time Domain

As we mentioned in the previous chapter, observing the time history of the pressure recorded by the microphones does not allow us to distinguish the most significant noise components in this setup. However, we know that the noise from a propeller manifests as peaks or valleys of pressure, with amplitudes that vary depending on the distance from the source. In this section, we will use the time data recorded by the four axial microphones to evaluate the pressure attenuation coefficients along the axis of the duct.

The four axial microphones were obtained by aligning the microphones placed along the circumference with the module dedicated to the three axial microphones. In the following Figure, we present the time signal acquired and calibrated by these microphones
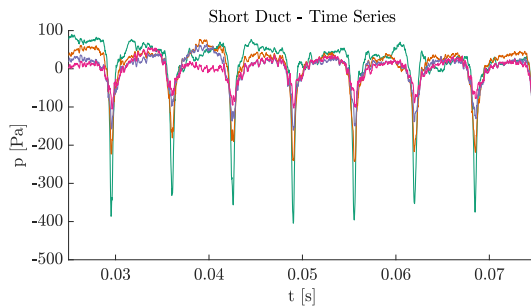
Figure 4.7: Time series - short duct   Figure 4.8: Time series - long duct
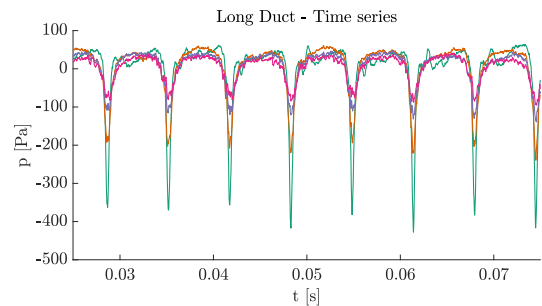
When the microphone is positioned in front of the propeller blades (in the direction of its motion), we can observe pressure valleys. As the propeller blade rotates, it interacts with the air. When the microphone is positioned in front of the blade the airflow generated by the rotation of the blade will cause a decrease in pressure in front of it. This drop in pressure corresponds to a pressure valley as the air is sucked toward the blade. In terms of fluid dynamics, the blade is pulling air towards itself, creating a low-pressure area, which the microphone detects as a valley in the pressure signal. Over the course of a full rotation, each blade passes in front of the microphone at regular intervals. From the following plot Figure (4.9) we can see how the time signal changes when the axial microphones are located upstream, overhead and downstream the propeller plane.

42
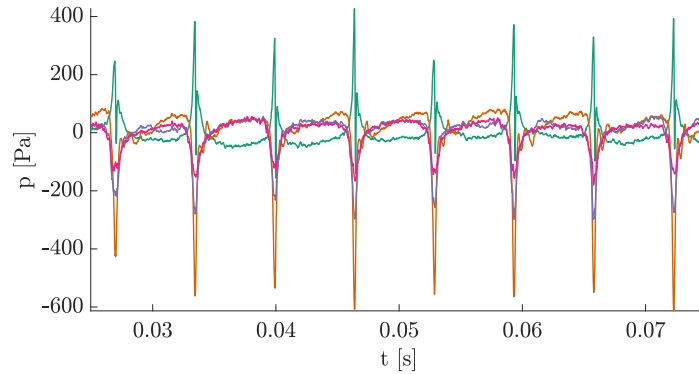
Figure 4.9: Time series form the setup 3.

When the microphone is positioned behind the propeller blade (relative to its direction of rotation), we observe pressure peaks rather than pressure valleys. This can be explained by considering the interaction between the blade and the air, and how this affects the microphone's pressure readings. If the microphone is located behind the blade, the airflow produced by the blade is actually pushing the air towards the microphone. The microphone detects this increase in air density, which is interpreted as a compression and shows up as a pressure peak.

Having explained the meaning behind these pressure peaks and troughs, we can look at how the signal is changing if we move along the duct axis. The four axial microphones span a total length of about $5cm$. The one nearest to the propeller plane is approximately $35mm$ distant from it, while the furthest is about $85mm$ away. As the microphone gets closer to the propeller plane, the absolute magnitude of the pressure spikes and troughs increases, and the pressure valleys and peaks become narrower.

We are now interested in looking how the signal acquired from these microphones decades along the duct axis, moving away from the propeller plane towards the duct inlet. Using the envelope function in MATLAB, we can determine the value of each of these pressure valleys.
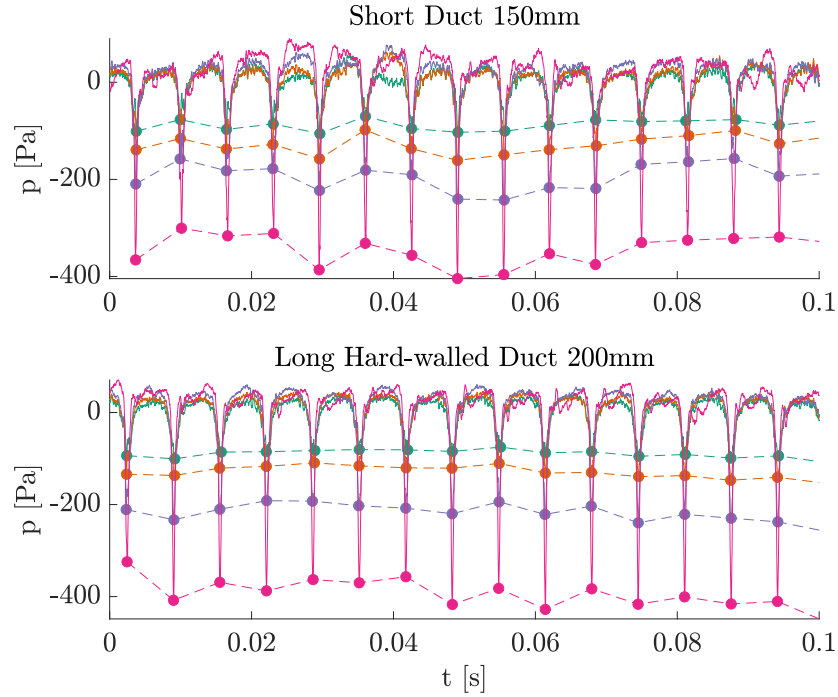
Figure 4.10: Detection of $p_{troughs}$

It is observed that the values of these depressions do not fluctuate significantly, so once these values are recorded, the data is averaged. The process is repeated for each of the four axial microphones. Since the long and short duct configurations are slightly different the microphones are not placed at the same distance from the propellers blade. The exponential decay you observe in the pressure values as you move away from the plane of the propeller blade can be explained by several principles of acoustic, particularly sound wave propagation and attenuation of sound pressure with distance and visco-thermal dissipation. When the propeller blade passes near the microphone, it generates sound waves that propagate through the air. The intensity of these sound waves depends on the distance from the source (the blade). As we move further from the source, the pressure of the sound waves tends to decrease. The exponential decay law is typical of sound wave dissipation in a medium (such as air), where the sound energy is lost due to factors like air viscosity, sound absorption and interference.

$$P(x) = P_0 \exp\left(-\alpha x\right) \tag{4.2}$$

Where:

- $P(x)$ is the sound pressure at distance x from the blade

44
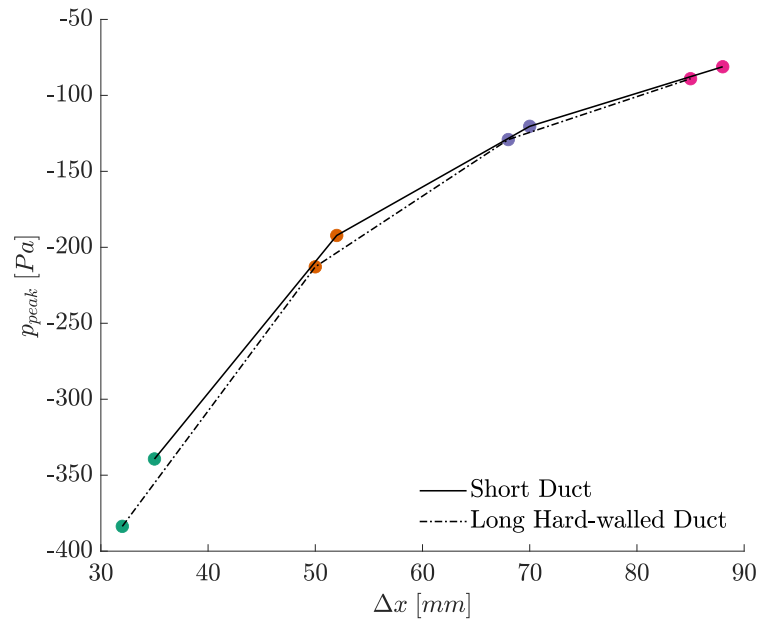
Figure 4.11: Decay of p_{mean} with distance from the propeller

- P_0 is the initial sound pressure (when the microphone is very close to the blade)

- α is the attenuation coefficient of the sound in air

- x is the distance from the plane of the propeller blade

In this case, as the sound propagates away from the blade, its energy is dissipated, and this dissipation is well-modeled by an exponential law, with the attenuation coefficient α depending on factors like the medium's properties and the source of sound. In addition to sound attenuation, the geometry of the duct could also influence how the pressure is distributed and decays with distance. This decay can be attributed to several factors:

- Energy dissipation: As the pressure wave propagates through the fluid, part of the energy is dissipated due to the fluid's viscosity and interactions with the duct walls.

- Expansion of the wavefront: As the distance from the blade increases, the wavefront expands over a larger surface area, causing a decrease in energy density and thus the pressure amplitude.

45

- Diffraction effects: The presence of obstacles or irregularities within the duct, such as gaps, can cause diffraction of the sound wave, dispersing the energy and attenuating the signal amplitude.

We could also see this exponential pattern modelled as

$$P(x) = P_0 \, exp(-x/\lambda) \tag{4.3}$$

Where:

- λ is the characteristic decay length

The following figures show the exponential fit that was performed on the measured data
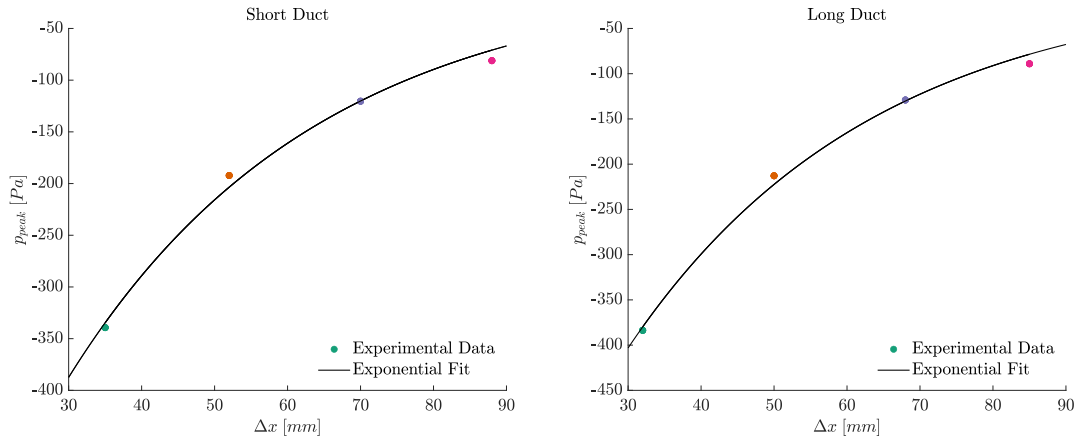
Figure 4.12: Exponential fit of the short and long duct configuration

The following table (4.1) presents the data related to the exponential fitting

Table 4.1: $P(x) = a \, e^{-\alpha x} = a \, e^{-\frac{x}{\lambda}}$

	a [Pa]	α [1/mm]	λ [mm]
Short Duct	-932	0.02926	34.2
Long Duct	-984	0.02974	33.6

The negligible variation in attenuation coefficients between the two duct configurations is not surprising. The axial microphones in both setups are positioned at nearly identical distances from the propeller, as evidenced by table (4.2). Due to the extremely close proximity of the source to the microphones, substantial

differences in attenuation are not observed.

We can now move to the frequency domain and analyze this same attenuation using the spectra. The following Figure (4.13) shows the SPL spectrum of the four axial microphones positioned inside the duct, upstream the propellers plane. $Mic1$ corresponds to the microphone farthest from the propeller (and therefore the closest to the inlet of the duct), while $Mic4$ is the closest to the propellers blade plane. The table (4.2) gives the information regarding the axial positions of the microphones relative to the propeller.

Table 4.2: Position of the axial microphones relative to the propellers plane expressed in $[mm]$

	$Mic1$	$Mic2$	$Mic3$	$Mic4$
Short Duct	88	70	52	35
Long Duct	85	68	50	32

As we move toward the propeller, we can see an increase in broadband and tonal noise.
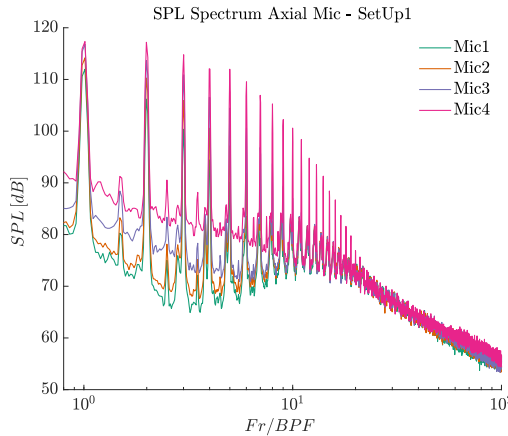
Figure 4.13: Short duct configuration   Figure 4.14: Long duct configuration
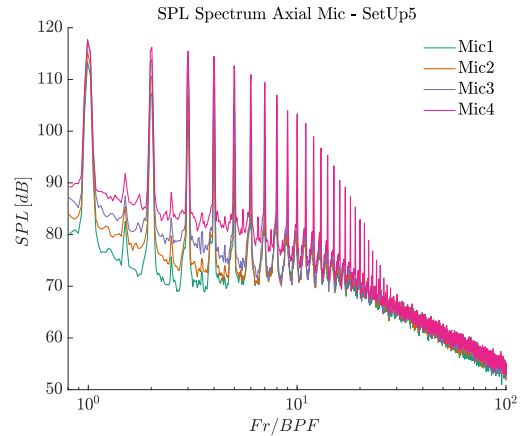
It is evident from Figure (4.15) that the long configuration has higher levels of sound, particularly visible in the broadband noise component that shows almost $5dB$ difference. In Figure (4.16) negative dB values indicate that the long duct has higher levels of noise.

47
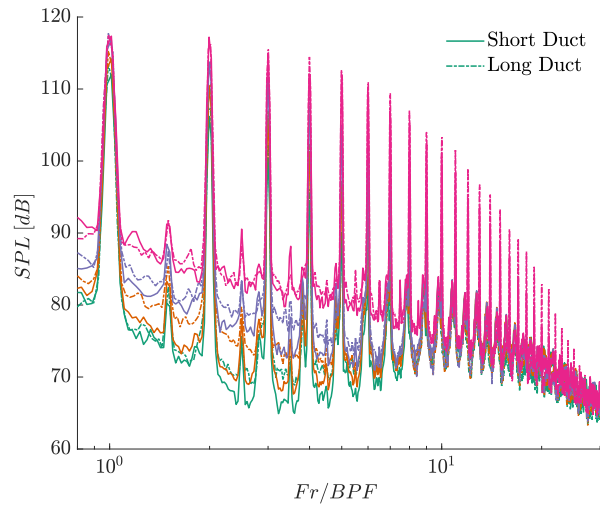
Figure 4.15: Comparison of the near-field SPL for the two configurations
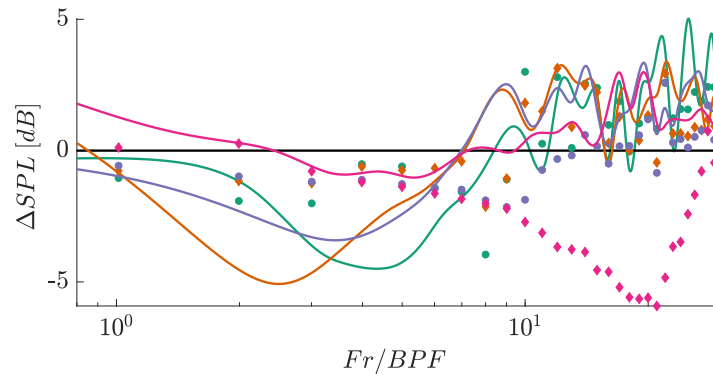
Figure 4.16: Comparison of the near-field sound power level for short and long shrouded setups. Broadband noise difference (solid lines), tonal noise difference (points)

For all the axial microphones, the longer setup shows higher values of broadband noise, which difference reaches its maximum between the second and sixth harmonic. Regarding tonal behavior, all microphones in the long duct exhibit higher levels for the first ten harmonics. The behavior of the fourth microphone, the one closest to the propeller, is the only one that differs. We observe that, compared to the other microphones, there are no significant variations in terms

48

of broadband noise (with maximum differences of 1 dB), and the tones follow a different pattern. As the frequency increases, the harmonics become increasingly prominent in the long duct. We attribute this response to the position of $Mic4$; as shown in table (4.2), this microphone is closer to the source.

Another way to observe the difference in sound levels between the two configurations is through a spectral map that shows how the SPL varies as a function of frequency and the distance from the sound source. The x-axis represents the distance between the microphone and the propeller, while the y-axis displays the frequency range.

In this image the SPL level recorded by each of the four microphones is represented using color, as a function of the microphone position (x-axis) and the frequency (y-axis). The figure highlights the combined effect of axial acoustic attenuation and the spectral dependence of the noise generated by the propeller. From the Figure, it is clearly evident that the SPL decreases with axial distance, especially at low frequencies. The tonal components of the propeller noise are evident as well-defined bands at frequencies corresponding to the Blade Passing Frequency BPF and its higher harmonics. Furthermore, it can be observed that the highest broadband noise levels are associated with low frequencies.
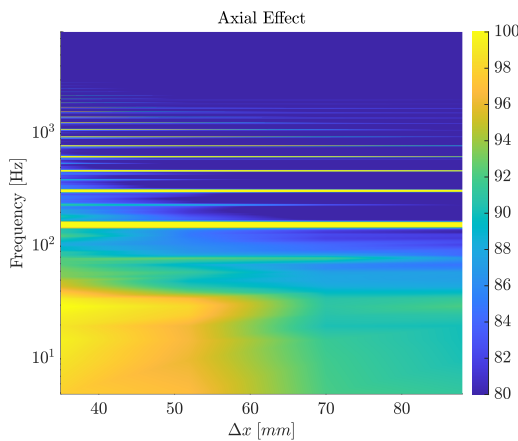
Figure 4.17: Short duct configuration   Figure 4.18: Long duct configuration
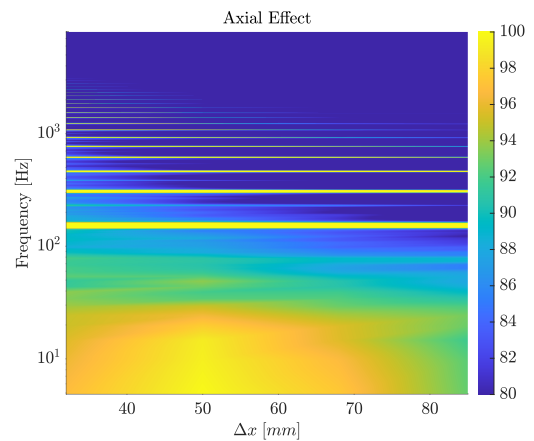
The long duct configuration (4.18) shows higher overall pressure levels compared to the short duct (4.17). Regarding the decay rate (attenuation of noise with the distance), high-energy regions in the long duct decay more gradually compared to the short duct. This may suggest that pressure fluctuations attenuate more slowly in the longer duct. In terms of frequency content, the long duct exhibits a wider range of high-intensity frequency content, extending to lower frequencies,

49

compared to the short duct. These differences indicate that the duct length significantly influences the aerodynamic and acoustic characteristics of the propeller-driven flow. The longer duct enables greater development of the unsteady pressure field, leading to more pronounced low-frequency content and slower decay of the high-pressure regions.

4.3.2 Decay Rates Inside the Duct

It is evident from Figures (4.19) and (4.20), which display the variation in broadband and harmonic noise between $Mic4$ and $Mic1$, respectively nearest and furthest from the source, that noise attenuation occurs from the microphone closest to the source to the one farthest away. Similarly to the time history analysis, it is of interest to examine the signal decay within the duct using the four axial microphones, in order to investigate the attenuation of noise. This time, being able to distinct and analyze specific range of frequency, we are focusing on the tonal noise in the low-mid frequency range $(1-5)$BPF.
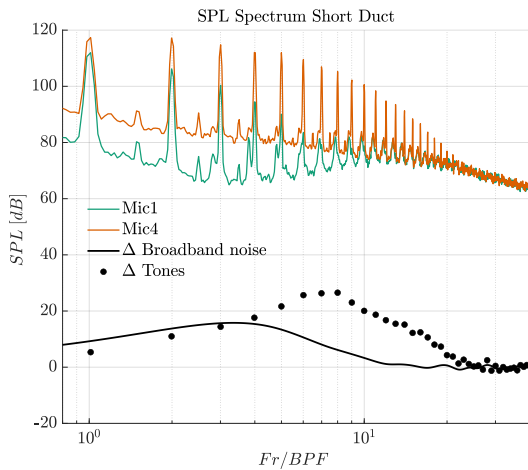
Figure 4.19: Short duct configuration   Figure 4.20: Long duct configuration
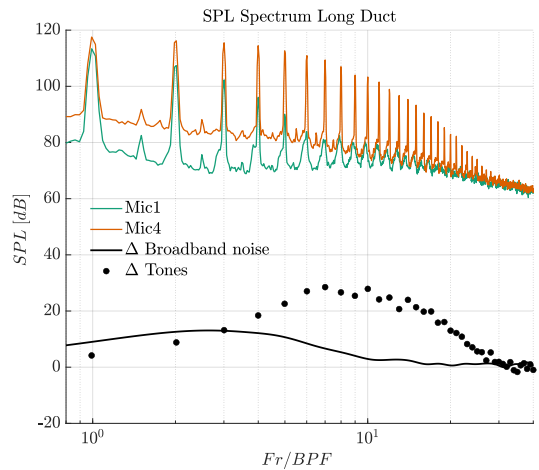
Figure 4.21: Decay Rate in the near-field

Our objective is to assess the decay rate of the first five tones along the four axial microphones. The values of the first five harmonics for each microphone are presented below, Figures (4.22),(4.23). To study the decay and evaluate the weight of each blade passing frequency, we plot the tonal value of the n-th BPF against the microphone position relative to the propeller plane.

50
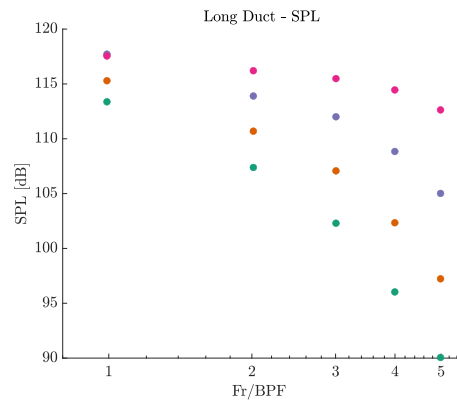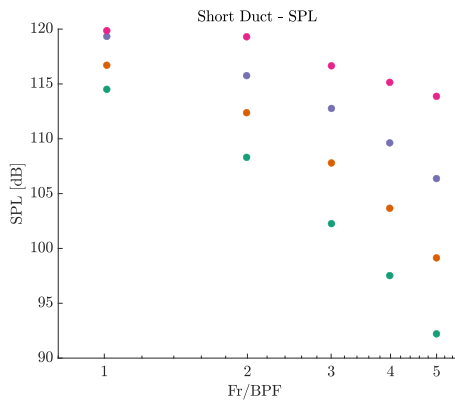
Figure 4.22: Short duct configuration   Figure 4.23: Long duct configuration

We can tell that the SPL generally decreases as the microphone is positioned further from the propeller, indicating attenuation of the pressure fluctuations, and that the decay rate varies across the harmonics. Lower harmonics (1st, 2nd BPF) show a more gradual decline in SPL, while higher harmonics exhibit steeper decay. For example, Figure (4.24) shows the first harmonic captured by the four axial microphones, plotted against the axial distance Δx from the propeller plane. To evaluate the attenuation of tonal noise, we performed a linear fit (first-degree polynomial) of the experimental data, obtaining the decay rate in dB/m corresponding to the slope of the fit. The procedure was repeated for both duct configurations
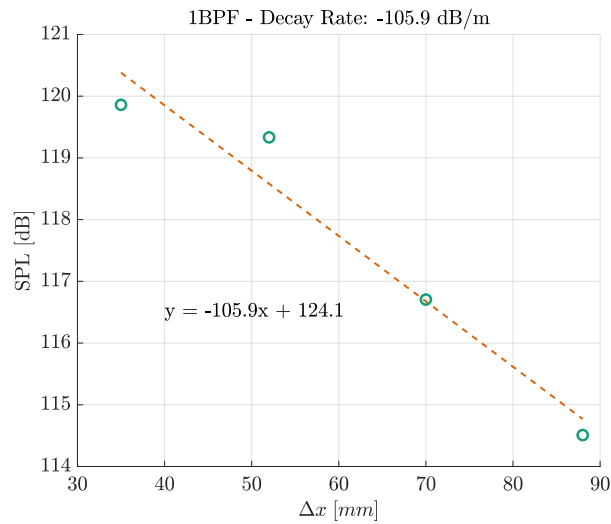
Figure 4.24: Decay rate of the first harmonic

51
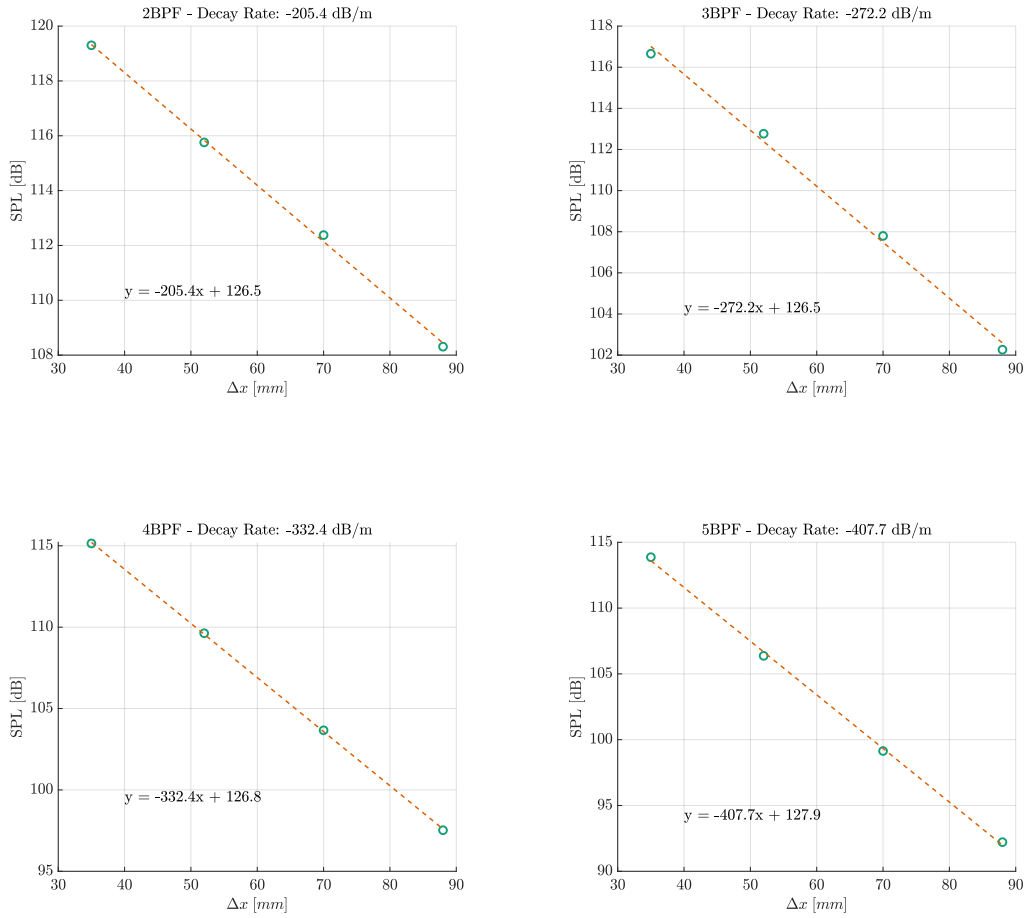
The following table (4.4) shows the decay rates for the five harmonics, comparing the values from the short and long ducts.

Table 4.3: Harmonics of the Blade Passing Frequencies for the short and long duct configurations [Hz]

BPF	Short Duct [Hz]	Long Duct [Hz]
1	156.2	151.4
2	307.6	307.6
3	463.9	459.0
4	615.2	610.4
5	771.5	761.7

Table 4.4: Tonal Decay Rates $[dB/m]$

BPF	Short Duct Decay Rates $[dB/m]$	Long Duct Decay Rates $[dB/m]$
1	-105.9	-84.5
2	-205.4	-167.2
3	-272.2	-250.8
4	-332.4	-346.5
5	-407.7	-424.0

A clear trend of increasing decay rate (in absolute value) is observed as the harmonic order increases. Higher harmonics attenuate more rapidly than the low frequencies, behavior consistent with the physics of duct acoustics, where high frequencies tend to attenuate more quickly due to viscous effects.

The different decay rates between the short and long ducts suggest the duct length impacts how the pressure fluctuations attenuate. Specifically, the steeper decay in the short duct, for example the second harmonic, indicates faster dissipation of the 2nd BPF pressure content. The more gradual decay in the long duct implies that the 2nd BPF harmonic is less attenuated over distance. This difference could be related to boundary layer effects, stronger flow separation or other unsteady effects:

- In the short duct, the boundary layer may develop more quickly, causing earlier flow separation and faster pressure attenuation.

- The longer duct allows the boundary layer to grow more gradually, potentially delaying flow separation and leading to slower decay of the pressure fluctuations.

The high-frequency tonal components are attenuated more effectively compared to low frequencies, and we can observe this behavior by plotting the decay rate as a function of frequency Figure (4.25).
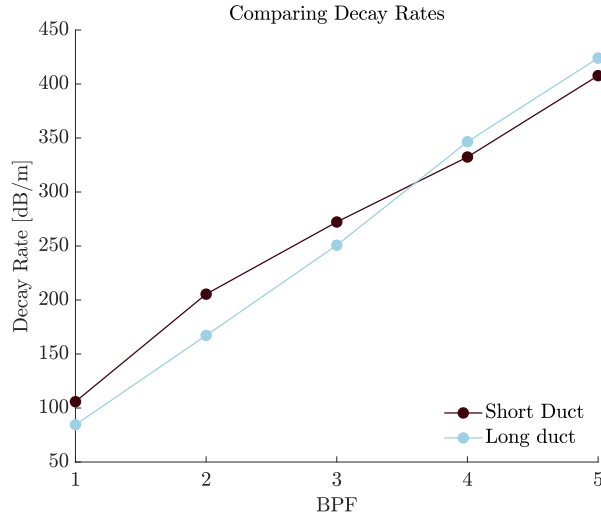
Figure 4.25: Comparing Decay Rates $[dB/m\,Hz]$

4.3.3 Coherence Spectra

In the field of signal processing, coherence measures the degree of similarity between two signals in the frequency domain. Coherence is a measure that quantifies the degree of linear correlation between two signals at a given frequency. Mathematically, the coherence function between two signals $x(t)$ and $y(t)$ is defined as:

$$\psi(fr) = \frac{|\phi_{xy}(fr)|}{\sqrt{\phi_x(fr)\,\phi_y(fr)}} \tag{4.4}$$

Where:

- $\phi_{xy}(fr)$ is the Cross-Power Spectral Density $CPSD$ between the two signals $x(t)$ and $y(t)$

- $\phi_x(fr)$ is the Power Spectral Density PSD of $x(t)$

- $\phi_y(fr)$ is the Power Spectral Density PSD of $y(t)$

The coherence value ranges from 0 to 1, where 1 indicates perfect linear correlation at frequency fr, while 0 indicates that there is no correlation between the two signals. There are few key reasons that make coherence useful in an aeroacoustic context:

- Source Identification: by examining the coherence between the microphone signals, we can identify the dominant noise sources within the system. Regions of high coherence typically indicate the presence of a strong, correlated noise source, while regions of low coherence suggest the presence of uncorrelated, broadband noise sources.

- Coherence can also help determine how sound propagates from the source to the measurement locations

The following Figures (4.26) (4.27) depict the coherence spectrum and its phase, calculated for both setups. From the magnitude of the coherence, it can be observed that for microphones positioned consecutively ($\Delta x = 18 \times 10^{-3}m$), a good correlation (0.8-1) is obtained up to frequencies of about 5000 Hz. This suggests that there are coherent noise sources present in this low-frequency region. As we move towards higher frequencies, the correlation value decreases.

Another variable affecting the correlation between two signals is the distance between them: if we consider microphones positioned at a distance of $2\Delta x$ or $3\Delta x$, the coherence decreases at lower frequencies. Faster drop in coherence for more distant microphones highlights that noise energy is attenuated more as it propagates along the duct, likely due to visco-thermal losses, reflections, or scattering effects. This behavior is consistent with the decay rates results that we obtained (4.25). Higher frequencies are more susceptible to attenuation and interference effects, which explains the faster coherence drop-off for distant microphone pairs.

The phase plot represents the phase difference between the two signals as a function of frequency. Linear phase trends at higher frequencies indicate a consistent time delay between microphones. The slope of the phase spectra corresponds to the propagation delay between the microphone pairs, that explains why there is a more pronounced phase difference for distant microphones. The larger separation between non-adjacent microphones introduces greater delays, leading to steeper slopes in the phase spectra.

The phase spectra at lower frequencies appears to have flatter slopes Figure (4.28), making it harder to detect a clear trend. This can be explained by:

- Proximity Effect : at low frequencies, the wavelength of the signal is greater than the distance between the two microphones. Longer wavelengths at low frequencies means that the phase difference between microphones becomes less significant compared to the spacing.

- Potential external influences (such as duct vibrations or boundary layer effects) that dominate the low-frequency range, adding noise to the phase calculation.
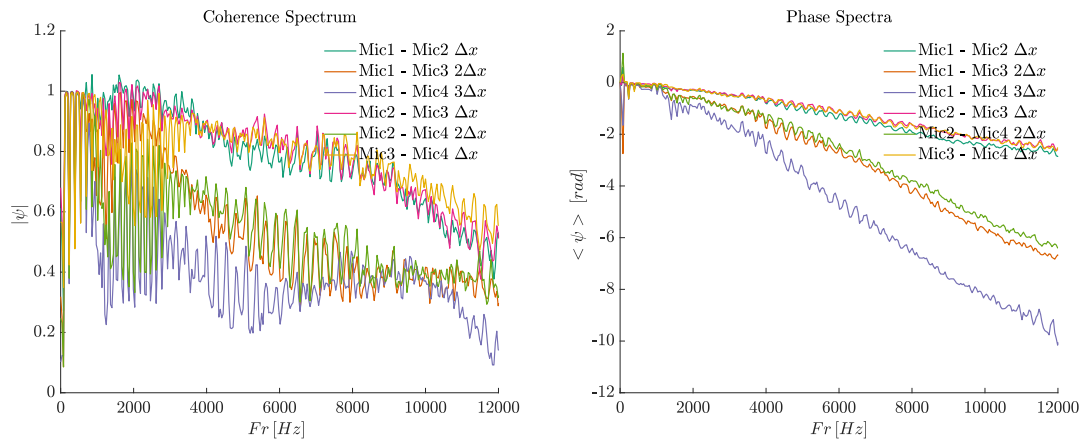
Figure 4.26: Coherence magnitude and phase spectra of the short duct configuration
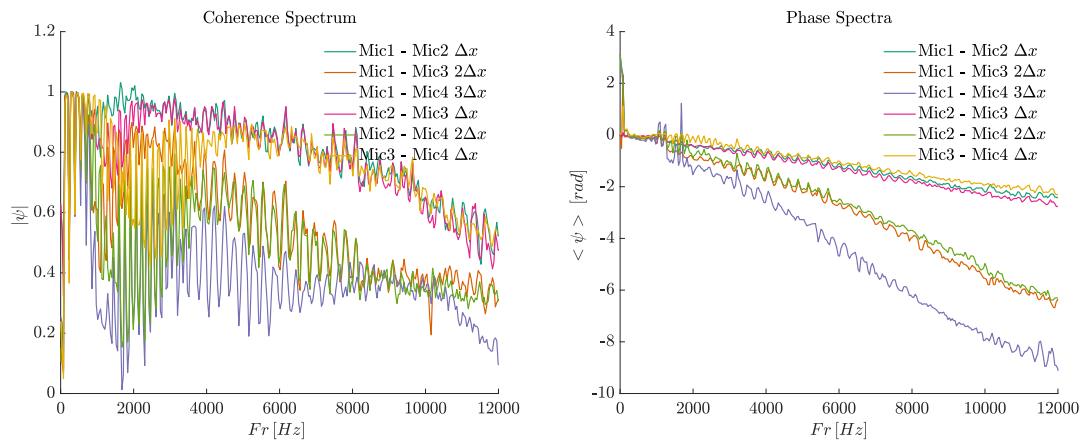
Figure 4.27: Coherence magnitude and phase spectra of the long duct configuration
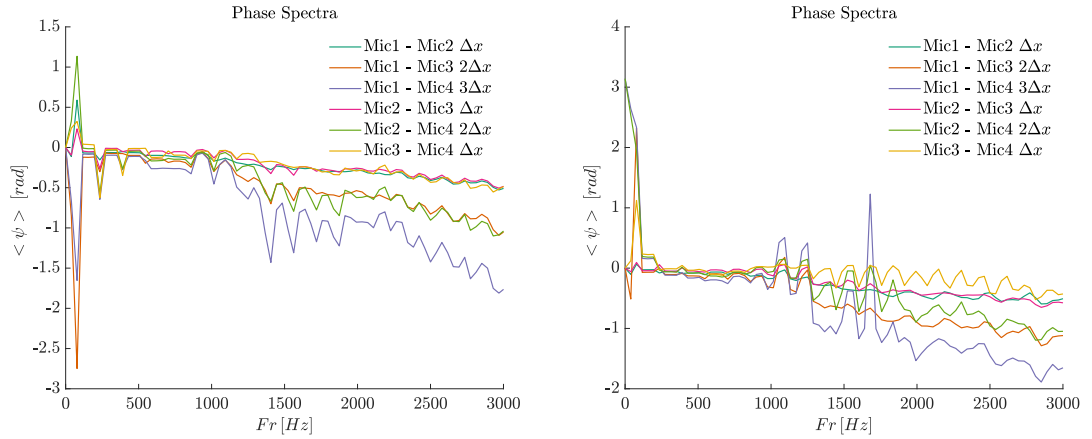
Figure 4.28: Zoom of the phase spectra at lower frequencies

4.4 Azimuthal Microphones

Now we focus our attention on the microphones positioned along the semi-circumference of the duct. In this section, we will see how to use the signals from these microphones to measure the Mach number at the blade tip, performing the calculation both in the time domain and in the frequency domain. We then used these microphones to observe how the SPL levels are distributed along the circumference of the duct as a function of frequency. Their arrangement inside the duct also allowed us to perform a modal decomposition, which we visualize using a Joppa plot. With this final step, we identify the most significant circumferential modes in terms of noise propagation in our setup.

The pressure data recorded by the microphones positioned around the propeller blade can be utilized to estimate the Mach tip number. For better clearance, we plotted time signals recorded by just 3 of the 22 circumferential microphones. The pressure troughs recorded by the microphones positioned around the blade's circumference were used to estimate the time delay Δt.

$$\Delta t \simeq 2.75 \times 10^{-4} \, [s]$$

The Mach tip number is determined using the radius of the duct d, the speed of sound c and the distance between two subsequent circumferential microphones $2\pi/45$, where 45 is the total number of microphones that can be allocated on the circumferential module

$$M_{tip} = \frac{2\pi \, d}{c \, \Delta t \, 45} = 0.303 \tag{4.5}$$

57
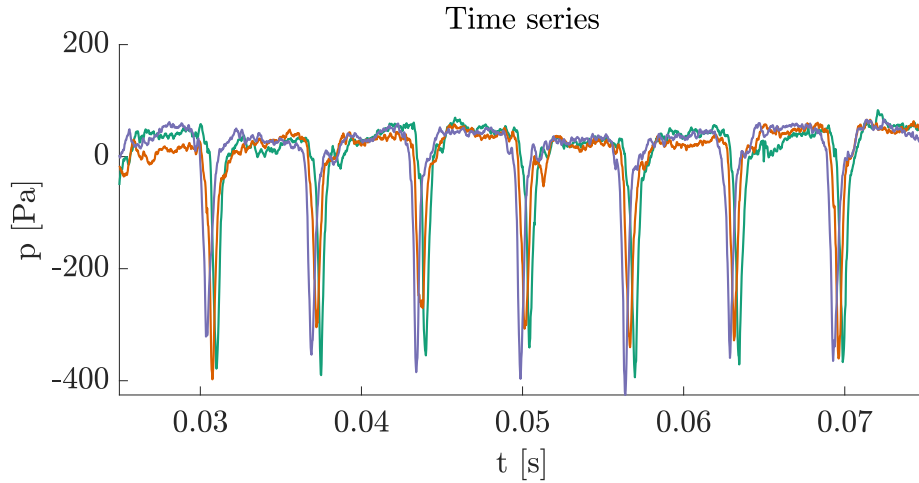
Figure 4.29: Time signal acquired from 3 circumferential microphones

It is important to note that the axial position of these microphones relative to the propeller differs between the short and long duct setups. When comparing the results obtained from these microphones, we evaluate not only the effect of duct length but also an attenuation effect of the signal, due to the fact that the module containing these microphones is located at different axial positions in the two setups.

Table 4.5: Distance of the azimuthal microphones from source and intake of the duct in the two setups

	Short Duct	Long Duct
Propeller plane	$35mm$	$85mm$
Intake	$70mm$	$70mm$

The following spectral maps are presented (4.30) (4.31). Similar to the process carried out to evaluate the 'axial effect' in the previous section, in this case we show how the SPL value varies as a function of frequency and azimuthal angle. Since the microphones in the long duct are located 50 mm more upstream compared to the short duct case, Figure (4.31) shows a visibly different behavior in terms of both tonal noise and broadband noise. The tonal component, clearly visible as high-energy horizontal bands at the BPF and its harmonics, is more pronounced in the short duct. Noise in these harmonics decays faster with frequency in the long duct. The low-frequency spectrum $(0 - 100$ Hz$)$ reveals lower energy levels and a different azimuthal distribution for the long duct. The noise distribution around

58

the duct is highly non-uniform, with up to 10 dB variations along the azimuthal angle. This low-frequency noise pattern cannot be attributed to axial attenuation. Aerodynamic turbulence, such as boundary layer separation or non-uniformities in the impinging flow, is a possible explanation.
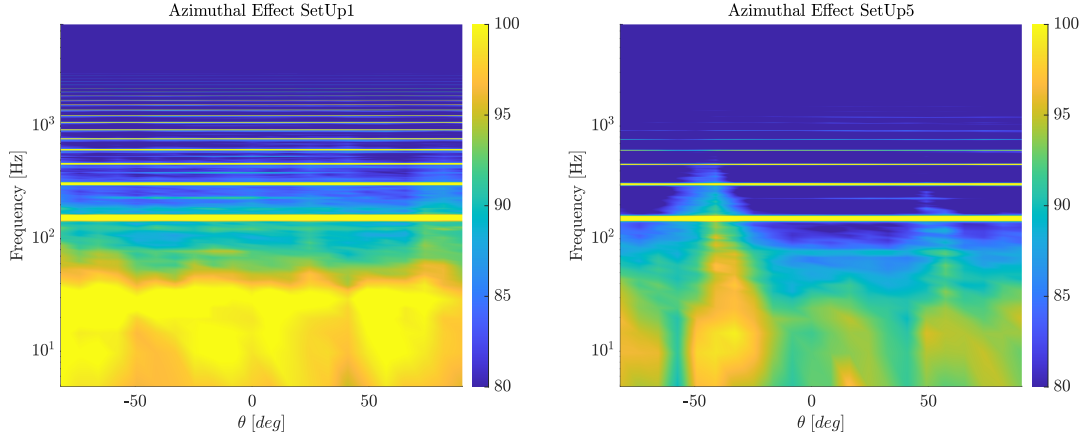
Figure 4.30: Azimuthal effect for short duct configuration

Figure 4.31: Azimuthal effect for long duct configuration

4.4.1 Mach tip number - Frequency Domain

To more accurately determine the tip Mach number, we employ the coherence spectrum phase. For this measurement, the circumferential module was positioned on top of the blade plane. Figure (4.32) shows an interesting result: the signal remains highly correlated $(0.8 - 1)$ between microphones at both high and low frequencies, due to the fact that all microphones are positioned on the source plane. The phase spectrum displays a clean linear trend, confirming this strong correlation. As previously mentioned, the slope of the coherence phase is related to the signal propagation delay. We can describe this linear dependence between coherence phase and frequency as:

$$\Delta < \psi >= -2\pi\Delta f \frac{\Delta x}{c} \qquad \Longrightarrow \qquad \frac{\Delta < \psi >}{-2\pi\Delta f} = \frac{\Delta x}{c} \qquad (4.6)$$

Where:

- Δx is the distance between two microphones

- c speed at which the correlated signal is propagating

The following table shows the time delay evaluated from the spectra

Table 4.6: Time Delay evaluated from Coherence phase spectra

Distance mic	Δt [s]
$\Delta\theta$	2.83×10^{-4}s
$2\Delta\theta$	2.78×10^{-4}s

$$M_{tip} = \frac{2\pi \, d}{c \, \Delta t \, 45} = 0.3 \tag{4.7}$$
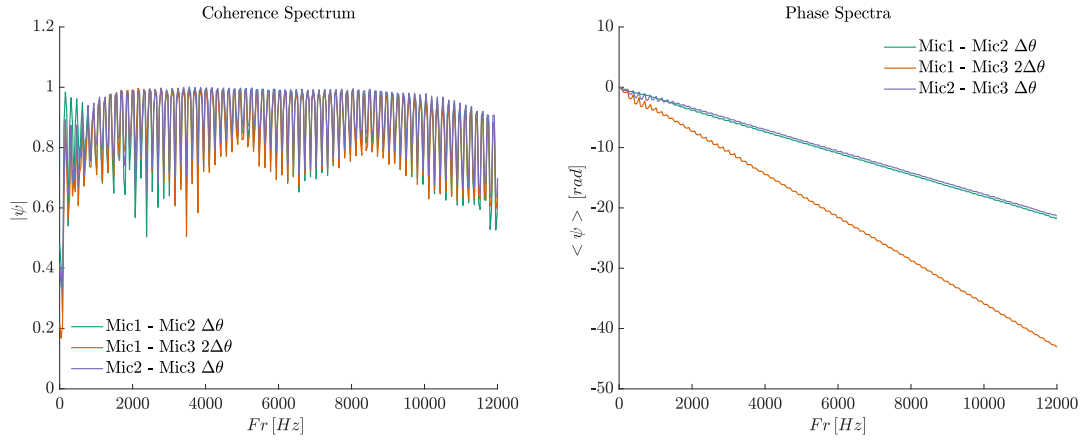
Figure 4.32: Coherence spectra - Azimuthal microphones

Figure 4.33: Coherence phase spectra - Azimuthal microphones

4.4.2 Modal Decomposition

Modal decomposition is a key tool in the analysis of noise generation and propagation in ducted propeller systems. By breaking down the acoustic field into individual modes, it enables the identification of dominant noise sources and their propagation characteristics within the duct. This approach is particularly useful for understanding how the duct geometry and propeller operation condition influence noise distribution. The use of upstream microphones, positioned along a semicircular array, allows for precise spatial and spectral measurements of the sound field. The 22 microphones, evenly spaced around half circumference of the duct, were used to visualize the circumferential mode patterns of the acoustic field inside the duct. The amplitudes of the different circumferential harmonics

(m-orders) at $(z, r) = (z_l, a)$ can be estimated as (Venkateswaran et al., 2024):

$$p_m(z_l, a, \omega) = \frac{1}{N} \sum_{s=l}^{N} p(z_l, a, \theta_s, \omega) e^{-jm\theta_s} \tag{4.8}$$

The Figure (4.34) shows a V-shaped pattern, indicating that at lower frequencies
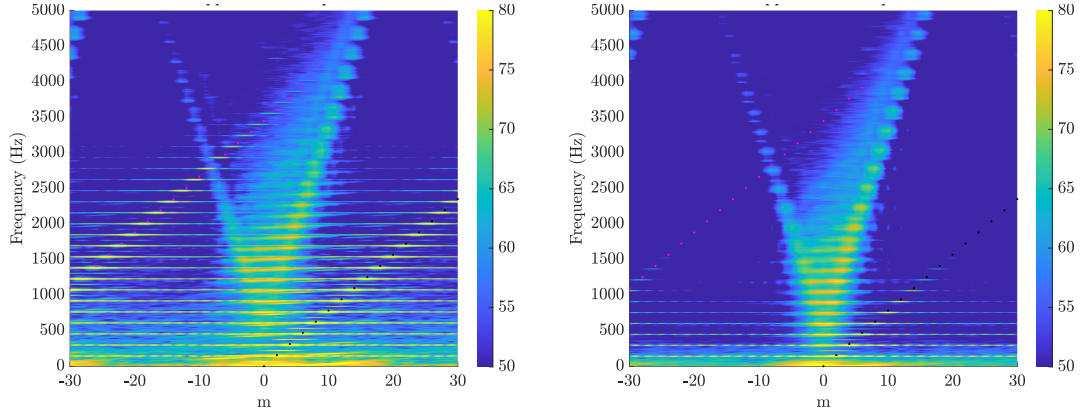
Figure 4.34: Joppa plot for the short (left) and long (right) configurations

only low-order modes propagate. The strongest acoustic content is concentrated for lower modes ($m = -5$ to $m = 5$) at lower frequencies. The energy is concentrated in the lower frequency regions, up to around $2000Hz$. This suggests that the primary sources of noise are related to large-scale flow phenomena and blade passage effects, rather than high-frequency turbulence-induced noise. The energy content decreases as we move towards higher frequencies and higher mode numbers.

The symmetry of the plot could tell us that the convective effects of the mean flow might be too small to affect the propagation of acoustic modes. The symmetry suggests also that there is no preferential direction for the acoustic wave rotation in the duct, meaning that there are similar amplitude levels and patterns for both positive and negative circumferential modes.

In the Figures we can visualize distinct points of high intensity (yellow regions) which represent the blade passing frequency harmonics. The differences between the two Joppa plots are more likely related to the microphone positions relative to the propeller plane rather than the duct length. In the short configuration, the microphones are positioned upstream of the propeller at a distance of $35mm$, while in the long configuration, the circumferential microphones are located $85mm$ from the propeller plane.

The right plot demonstrates more concentrated energy around lower mode numbers and exhibits a clearer cut-off behavior compared to the short duct setup

(left plot). The larger distance from the propeller in the long configuration causes evanescent (non-propagating) modes to weaken significantly. Additionally, the flow noise or hydrodynamic noise is less contaminated, resulting in measurements at $85mm$ that provide a more "far-field" representation. This observation suggests that microphone positioning is critical for capturing different aspects of the acoustic field.

A clear presence of rotor-locked modes is observed in the short configuration. The plot highlights prominent diagonal patterns corresponding to the Blade Passing Frequency (BPF) of the two-bladed propeller and its harmonics. The BPF represents the periodic interaction between the propeller blades and the surrounding air, manifesting as strong acoustic modes at discrete frequencies. The overlaid points indicate the positions of the BPF and its harmonics, confirming that the energy concentrates along these patterns. These modes are subsonic and do not radiate.

Chapter 5

Liner Effect on Noise Measurements

This chapter will explore the impact of a Over-Tip-Rotor (OTR) acoustic liner applied to the duct's inner surface, comparing the findings with the baseline case of the long hard-walled duct. The passive acoustic treatment is a grooved liner in which the annular grooves are filled with a metal foam of Nickel Chromium Alloy flush with the shroud inner wall. A summary of the liner design parameters is shown in table (5.1), where POA is the Percentage Open Area, h is the cavity depth and σ is the porosity of the metal foam.

Table 5.1: Liner design parameters

Liner	Type	$h\,[mm]$	$POA[\%]$	$\sigma\,[\%]$
Grooved	semi-locally reacting	17.5	44	90

The liner is locally reacting in the axial direction and non-locally reacting in the azimuthal direction. Note that this POA only accounts for the grooved area relative to the total liner area and not the open area of the metal foam within the grooves. The paper presented by Palleja-Cabre et al., 2024, has investigated experimentally the reduction of noise in shrouded propellers by using two different types of Over-Tip-Rotor (OTR) liners. Experimental far-field noise data has been presented for SDOF and grooved metal foam liners tested with a bellmouth intake and a lip or unflanged intake. It was also assessed how noise reduction performance is affected by the position of the liners, comparing the OTR results with data obtained when the liners are placed upstream and downstream of the propeller plane. It can also be found a sectional analysis of the OTR grooved liner configuration.

5.1   Far-Field Noise Measurements

In this section, we are going to analyze and compare the how the far-field acoustic radiation is affected by the presence of the OTR liner inside the duct, comparing the baseline configuration an the acoustic treated case.

To better understand the difference in the spectra of the two setups, Figure (5.1) shows the SPL in the far-field measured from the hard-walled duct configuration (solid lines) and the lined duct configuration (dashed lines). Even by simply
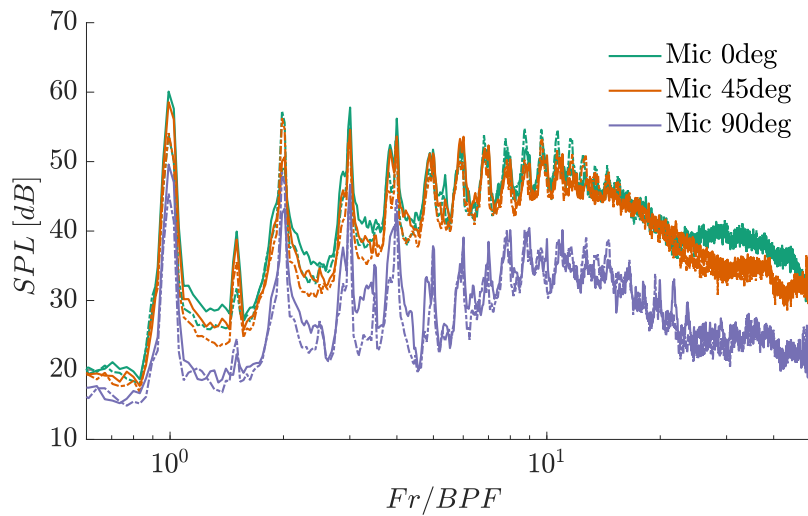
Figure 5.1: Comparison of the sound power level for hard-wall (solid lines) and liner (dashed lines) shrouded setups

looking at the spectrum, we can observe that the presence of the liner leads to a reduction in broadband noise, but to gain a more accurate understanding of what happens in terms of tonal noise, we refer to Figure (5.2). Figure (5.2) shows the difference in broadband and tonal noise from the two configurations, for all three far-field microphones. Positive values indicate that the liner has produced an attenuation of noise with respect to the baseline configuration, while negative values show that the lined duct produces higher sound levels.

In terms of broadband noise, all three microphones show a reduction, about $2-3dB$, when adding the liner on top of the propeller. The microphone positioned along the rotation axis of the propeller exhibits slightly different behavior. The broadband noise is not significantly affected by the presence of the liner at low frequencies; however, a greater effect is observed increasing frequencies, with a
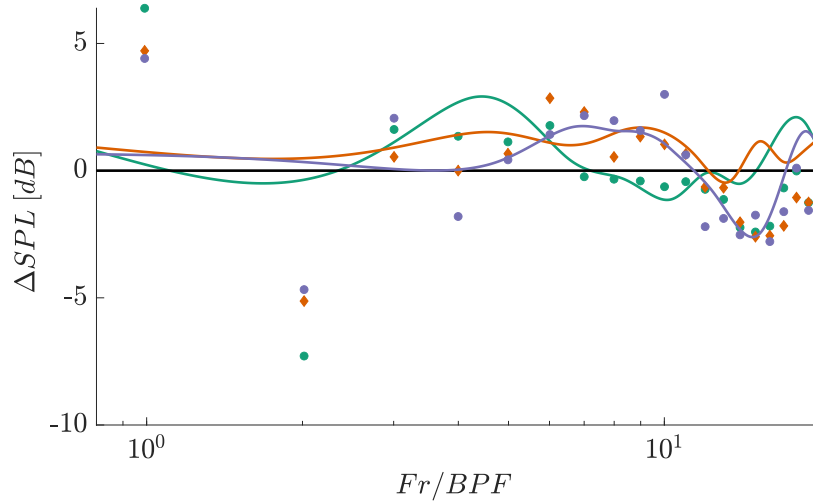
64

Figure 5.2: Comparison of the sound power level of hard-walled and lined shrouded setups. Broadband noise difference (solid lines), tonal noise difference (points)

reduction of approximately $3dB$ around the $4th$ harmonic. At higher frequencies, the difference between the two configurations is not so clear, oscillating around zero.

Regarding tonal noise, all the FF microphones show a similar pattern for the first 2 harmonics: the first BPF is the frequency where we can appreciate the higher reduction of noise, approximately $5dB$. Conversely, the second BPF has an important increase of noise, adding about $5 - 7dB$ when placing the liner. As we move toward higher frequencies, the liner configuration seems to produce small reductions in tonal noise $(1 - 3dB)$. Beyond the tenth harmonic, the configuration with the liner appears to have a more significant tonal component compared to the baseline configuration. As we saw in the previous Chapter, the FF noise spectrum of the long configuration showed that after the first 10BPFs the noise spectra is mainly due to broadband noise.

5.2 Near-Field Noise Measurements from Axial Microphones

As we did in the previous chapter, we are now going to compare the near-field noise measurements made by the two setups. After examining how the presence of the liner affects far-field radiation, we use the microphones inside the duct to observe

the liner's effect in the near field. Given the proximity of the microphones, which in the previous chapter raised some doubts (e.g., in the calculation of decay rates) about how sound waves propagate inside the duct, it now becomes an advantage in understanding the behavior of the liner. It is worth noting that both of these two configurations are 'long ducts', meaning that the total length of the setup is the same $230mm$, and also the relative position of the inside-duct microphones to the source is the same (4.2). The following Figure (5.3) shows the SPL spectrum of the four axial microphones positioned inside the duct, upstream the propellers plane. It is evident that the untreated configuration produces higher levels of sound, particularly visible in the broadband noise that shows almost $6dB$ difference.
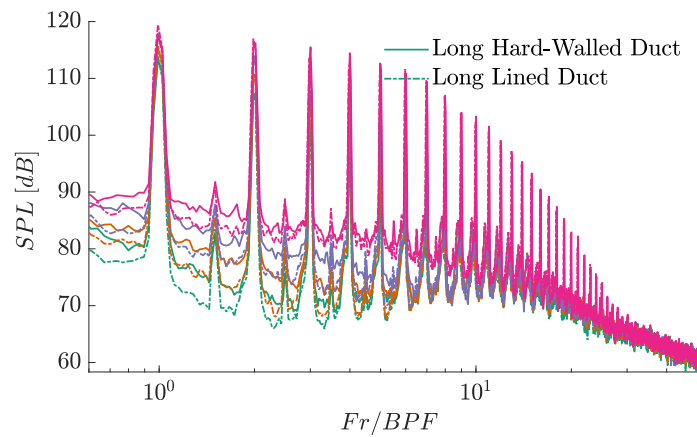
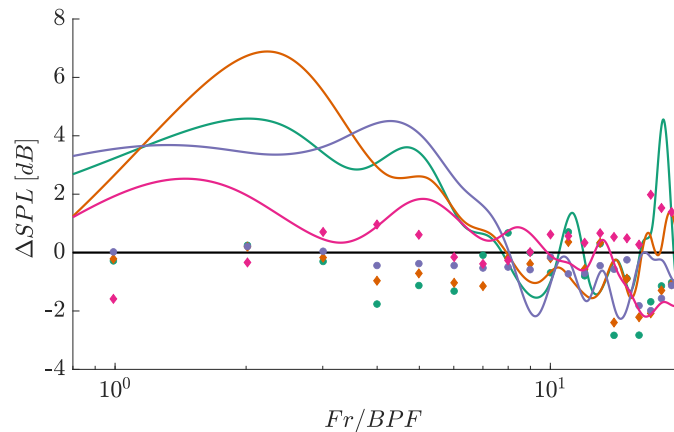Figure 5.3: Comparison of the near-field SPL for the two configurations

Figure 5.4: Comparison of the near-field SPL for the two configurations. Broadband noise difference (solid lines), tonal noise difference (points)

We can appreciate a relevant broadband noise reduction from Figure (5.4) in the range of the first 10 harmonics. As the frequency gets higher the difference in broadband noise oscillates around zero. Concerning tonal noise, there is no substantial differences between the two configurations, with values fluctuating near zero. The most noticeable effect of the liner is then on broadband noise at low-mid frequencies; the attenuation becomes more evident as the microphone moves farther from the source.

In the previous chapter, we examined the spectral map of the long rigid-walled duct configuration, noting a non-uniform distribution of sound energy levels at low frequencies. It is interesting to see if the configuration with the liner exhibits the same behavior. Figure (5.6) clearly demonstrates the effect of the liner, especially at low frequencies. Lower energy values are observed compared to the untreated configuration. Regarding sound attenuation along the duct axis, the liner configuration exhibits the same pattern as the short duct. Microphones closer to the source record higher SPL values compared to those farther away. When compared to the short duct setup (4.17), the configuration with the liner shows even more pronounced attenuation along the axis.
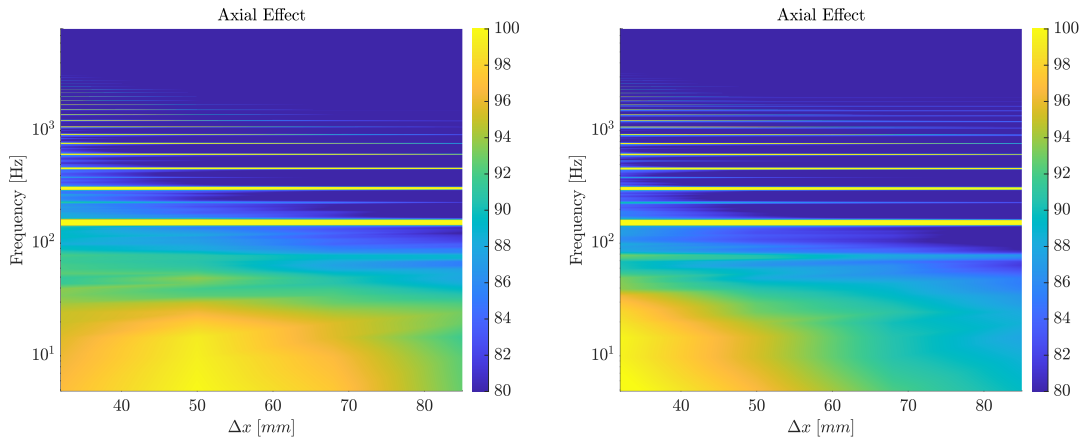
Figure 5.5: Long baseline duct configuration

Figure 5.6: Long lined duct configuration

To further analyze the low-frequency behavior, we examine the spectra presented in Figures (5.7) (5.8). These spectra depict the frequency content measured by the 4 axial microphones within the $0-200 Hz$ range. A strange behavior we had noticed in the spectral map (5.5) of the long rigid-walled duct was the lack of evident attenuation of the signal at low frequencies. The spectra reveals that $Mic4$ (the nearest to the source) exhibits an anomalous response at low frequencies,

displaying a lower sound level compared to microphones 2 and 3, despite being farther from the source. This discrepancy, not observed in the lined duct configuration (5.8), is attributed to potential experimental errors, such as microphone misplacement or vibrational interference.
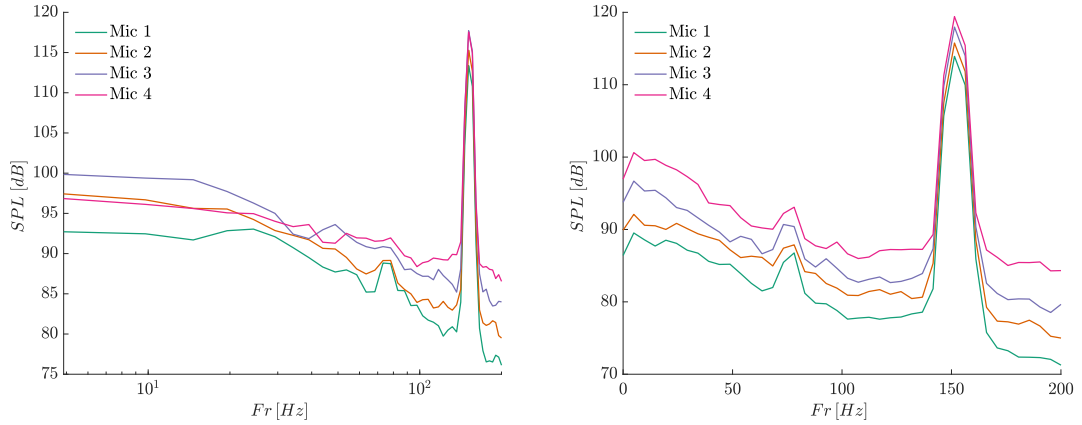
Figure 5.7: Low frequency Spectrum Long baseline duct configuration

Figure 5.8: Low frequency Spectrum Long lined duct configuration

The remaining microphones display expected behavior. To facilitate comparison of low-frequency SPL values, Figure (5.9) presents the SPL difference between the baseline and treated ducts. Positive values signify lower energy levels in the lined duct, while negative values indicate higher sound pressure levels. As we can see, Mic4 ($\Delta x = 32mm$) is $4dB$ more noisy in the lined configuration.
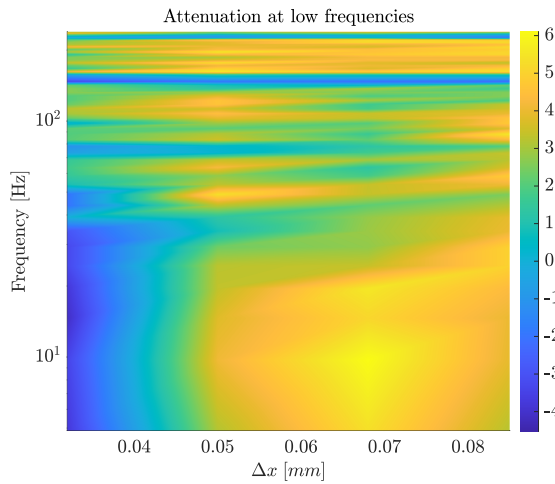

Figure 5.9: Low frequency Spectrum Long lined duct configuration

68

5.2.1 Decay Rates Inside the Duct

In order to assess changes in attenuation along the duct axis, we evaluate the decay rates for the first five harmonics. The procedure followed is the same as that presented in the previous chapter: a linear fit was used to estimate the attenuation coefficient for each harmonic. For example, Figure (5.10) shows how the first harmonic decays over $5cm$
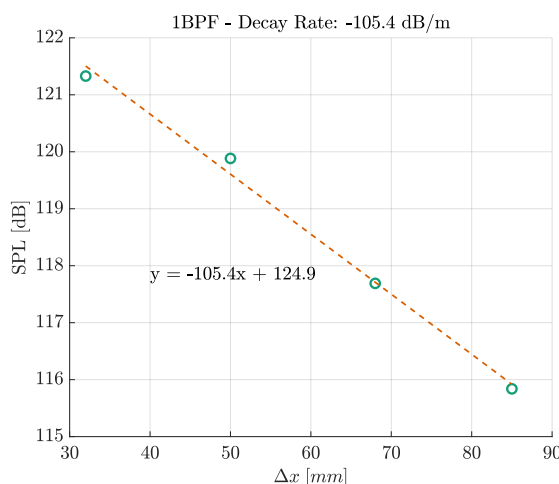
Figure 5.10: Decay rate of the first harmonic

The following table (5.2) summarizes the calculated decay rates for the three duct configurations: short, hard-walled and lined long ducts.

Table 5.2: Tonal Decay Rates $[dB/m]$

BPF	Short Duct	Long Untreated Duct	Long Lined Duct
1	-105.9	-84.5	-105.4
2	-205.4	-167.2	-177.1
3	-272.2	-250.8	-223.3
4	-332.4	-346.5	-297.4
5	-407.7	-424.0	-392.6

The trend is the same: increasing decay rates (in absolute value) with the harmonic order. The results Figure (5.11) indicate that the liner has a negligible effect on the attenuation of tonal noise at the first harmonics. It is crucial to note that these decay rates are not directly comparable to theoretically predicted attenuation values for cutoff modes inside the duct. The presence of an incoming

flow, which produces boundary layer and flow separation, leading to elevated turbulence intensity levels, coupled with the close proximity of the microphones to the source ($3cm$ from the propeller blade), may account for the significant attenuation observed in our data. This attenuation might be attributed to the persistence of evanescent acoustic modes (cut-off modes) in the vicinity of the microphones.
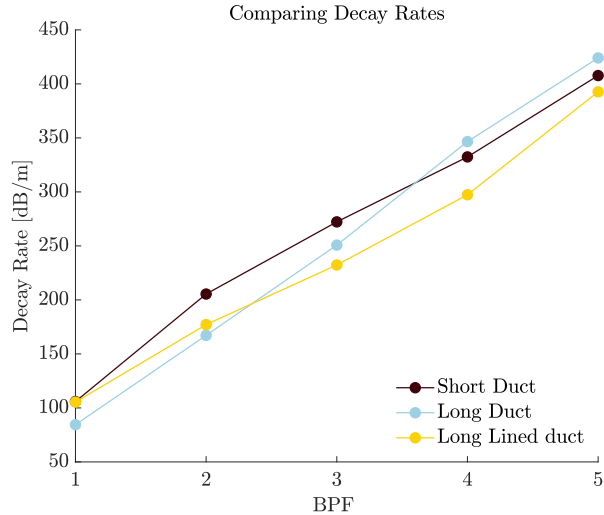
Figure 5.11: Comparing Decay Rates $[dB/m\,Hz]$

5.3 Near-Field Noise Measurements from Azimuthal Microphones

This time, the position of the circumferential module is the same in both setups. This implies that the decreased sound power levels observed in Figures (5.12) and (5.13) is solely attributable to the presence of the Over Tip Rotor liner. A significant noise attenuation, especially at low frequencies, is evident. We also note that the non-uniform acoustic pressure pattern in the baseline duct at low frequencies is still present, although less pronounced, in the configuration with the liner.

5.3.1 Modal Decomposition

The introduction of the liner has a visible effect in reducing the overall modal intensity, especially for modes with high azimuthal order $|m|$ and at intermediate frequencies. This demonstrates its ability to attenuate the noise propagating

Figure 5.12: Azimuthal effect for long duct configuration

Figure 5.13: Azimuthal effect for long lined duct configuration

within the duct. However, some low-frequency modes ($< 1000Hz$) are relatively less affected.

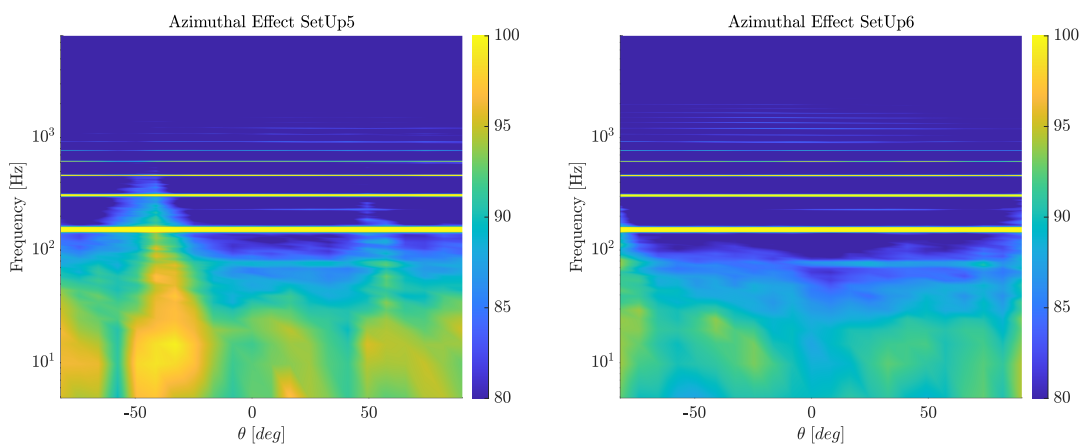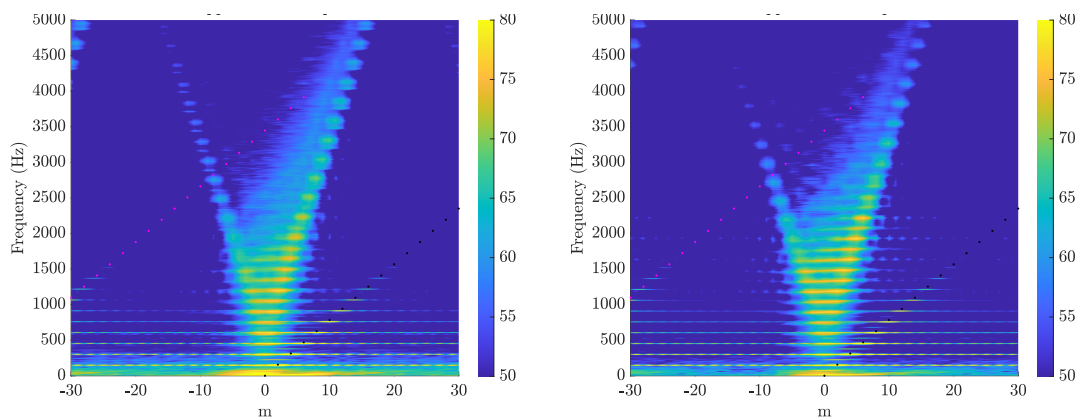Figure 5.14: Joppa plot for the long hard-walled duct (left) and long lined duct (right) configurations

71

Chapter 6

Conclusions and Future Works

In this experimental campaign, we investigated the sound generated by a shrouded propeller. Numerous experiments have been conducted in this area, evaluating the effects of intake geometry and the placement of acoustic treatments inside the duct, near the source. In our experiments, we focused on assessing the effect of duct length, remaining within the context of short ducts. The use of an unflanged intake geometry, which is unable to guide the flow into the duct without significant boundary layer separation and increased turbulence intensity, was identified as an important noise generator. Hot-wire anemometry measurements revealed the presence of a separated and highly turbulent flow near the duct wall. The interaction between this flow and the propeller blades is expected to increase noise levels, due to periodic chopping of eddies in the incoming flow (tonal noise) and turbulence-leading edge interaction noise (broadband noise).

Regarding acoustic measurements, we used three microphones positioned in the far field, enabling us to evaluate the differences in radiated sound between the short and long ducts. Contrary to theoretical predictions, the long duct exhibited greater broadband noise, especially for microphones positioned in front of the plane of the duct's open end (0° and 45° degrees). This unexpected result was attributed to the asymmetric axial positioning of the propeller within the duct. In the long duct, the source is not centered along the duct axis, likely causing constructive interference between waves propagating upstream and downstream.

Near-field measurements were also included in the experimental setup, making use of 25 microphones inside the duct. These microphones were positioned both along the axial direction and azimuthal angle.

The axial detection of noise was used to evaluate the decay of sound waves propagating within the duct. The four axial microphones revealed that noise attenuation along the duct axis was primarily concentrated at low frequencies. The decay rates of the first five harmonics showed significant noise attenuation, likely due to the excessive proximity of the microphones to the source. The microphones,

positioned $3cm$ from the propeller, are likely subjected to the complex sound field generated in the near field, which may still contain evanescent modes that have not yet attenuated. This result highlights the complexity of the problem, and underscores the importance of understanding how to optimize duct geometry to fully exploit the characteristics of the sound field generated by a propeller, with the aim of minimizing noise radiation.

Regarding the 22 circumferential microphones, positioned along the semi- circumference of the duct in front of the propeller, they allowed us to study how the sound level is distributed along the azimuthal angle as a function of frequency. Finally, a modal decomposition revealed that the first azimuthal modes, which propagate at low frequencies, are the most significant in terms of noise propagation within the duct.

The effect of an Over-Tip-Rotor placement of a grooved metal foam liner was also studied. The results showed a beneficial effect, particularly in terms of broadband noise, with up to $3dB$ of noise reduction in the far field. For tonal noise, the first harmonic was the most affected by the presence of the liner in the duct, showing up to $5dB$ of SPL reduction. Conversely, the second harmonic was excited by the porous material, exhibiting an increase of at least $5dB$. The axial microphones inside the duct highlighted the significant beneficial effect of the liner, achieving 2 to $7dB$ of broadband noise attenuation. The introduction of the liner also had a clear impact on reducing the overall modal intensity, particularly for circumferential modes with high azimuthal orders m and at intermediate frequencies, demonstrating its ability to attenuate noise propagating within the duct.

Furthermore, this dataset will provide a valuable reference for future numerical data. A numerical analysis will be done to delve deeper into the results obtained from these experiments. The study will investigate the fluid dynamics of the system, with the aim of understanding the role of the flow generated within the duct in noise generation. Explore how this separated flow interacts with the blade tips and how the subsequent scattering of vortices at the trailing edge contributes to noise generation. Additionally, the modal amplitudes from these measurements will be used to model far-field radiation and also compared against an analytical model for a rotating point source in short ducts.

Appendix A

Broadband and Tonal Noise

Many times, acoustic data in the frequency domain have been processed to distinguish the tonal component from the broadband noise component. This appendix presents the procedure used to perform this separation, using MATLAB software. Given the non-stationary and noisy nature of the signals, we employed the *pwelch* method for spectral analysis.

```matlab
F_s = 40000;   %[Hz];
window = 2^13;
[pxx,freq]=pwelch(sign.data_signal(:,[ch1,ch2,ch3]),
    hann(window,'periodic'),0,window,Fs);
SPL = 10*log10(pxx)-10*log10((2*10^-5)^2);
```

In order to better understand the role of tonal and broadband noise in the spectra of a general signal measured by one microphone, we can distinguish the two noise components by employing the envelope function in MATLAB, to extract broadband noise from the spectrum

```matlab
fin = 30;
i=1;
while i <= length(channels)

    [~,YLOWER(:,i)] = envelope(SPL(:,i),fin,'peak');
    SPL_BB(i,:) = YLOWER; %broadband noise
    i = i+1;

end
```

Tones are found at multiples of the blade passing frequency. Indices corresponding to the tonal peaks at harmonics of the shaft rotational frequency of the propeller are found in the frequency vector. Each tonal peak is formed by multiple frequency

components near the BPF harmonic, and the overall sound pressure level of the tone is calculated as the sum of these components.

```matlab
BPF = 2*RPM/60;
for iii=1:100
    df_BPF = abs(freq-iii*BPF);
    minIdx_BPF(1,iii) = find(df_BPF == min(df_BPF));
end
n = 1:100; %First 100BPF
for i =1:length(channels)
    for j = 1:length(n)
            Tone(j,i) = 10*log10(sum(10.^(SPL(minIdx_BPF
                (1,j)-1:minIdx_BPF(1,j)+1,i)/10)));
    end
end
```

As an example, Figure (A.1) shows the FF noise spectrum of a single microphone and its broadband noise and tones at multiples of the blade passing frequency.
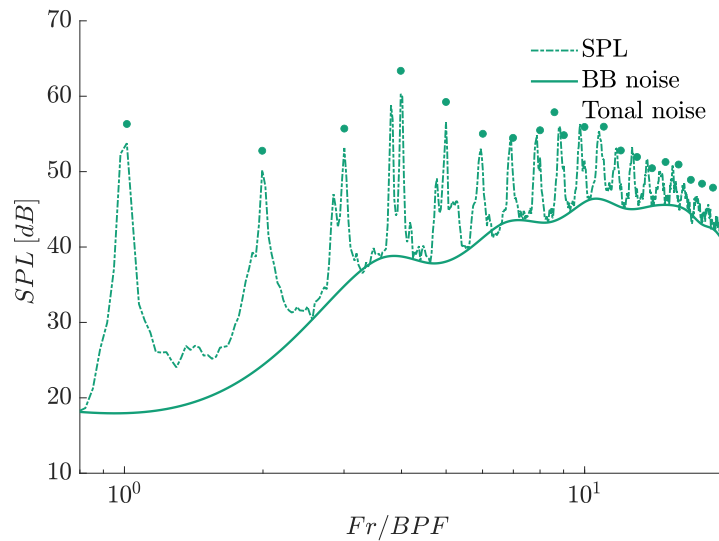

Figure A.1: Broadband and Tonal noise

Bibliography

Baddour, B., Joseph, P., McAlpine, A., & Leung, R. (2024). Duct effects on acoustic source radiation [Publisher: American Institute of Aeronautics and Astronautics _eprint: https://doi.org/10.2514/1.J063444]. *AIAA Journal*, *62*(3), 1037–1051. https://doi.org/10.2514/1.J063444

Glegg, S. A. L., & Devenport, W. J. (2017). *Aeroacoustics of low mach number flows: Fundamentals, analysis, and measurement*. Academic Press.

Go, S. T., Kingan, M. J., Wu, Y., & Sharma, R. N. (2023). Experimental and numerical investigation of the sound field produced by a shrouded UAV propeller. *Applied Acoustics*, *211*, 109523. https://doi.org/10.1016/j.apacoust.2023.109523

Malgoezar, A. M., Vieira, A., Snellen, M., Simons, D. G., & Veldhuis, L. L. (2019). Experimental characterization of noise radiation from a ducted propeller of an unmanned aerial vehicle. *International Journal of Aeroacoustics*, *18*(4), 372–391. https://doi.org/10.1177/1475472X19852952

Munjal, M. L., & Munjal, M. L. (2014). *Acoustics of ducts and mufflers* (Second edition (Online-Ausg.)). John Wiley & Sons, Inc.

Palleja-Cabre, S., Macey, E., Paruchuri, C. C., & Joseph, P. (2024). Reduction of shrouded propeller noise with over-tip-rotor liners. *30th AIAA/CEAS Aeroacoustics Conference (2024)*. https://doi.org/10.2514/6.2024-3407

Petricelli, F., Chaitanya, P., Palleja-Cabre, S., Meloni, S., Joseph, P. F., Karimian, A., Palani, S., & Camussi, R. (2023). An experimental investigation on the effect of in-flow distortions of propeller noise. *Applied Acoustics*, *214*, 109682. https://doi.org/10.1016/j.apacoust.2023.109682

Rienstra, S. W. (n.d.). Fundamentals of duct acoustics.

Rizzi, S. A. (2020). Urban air mobility noise: Current practice, gaps, and recommendations.

Romani, G., Grande, E., Avallone, F., Ragni, D., & Casalino, D. (2022). Performance and noise prediction of low-reynolds number propellers using the lattice-boltzmann method. *Aerospace Science and Technology*, *125*, 107086. https://doi.org/10.1016/j.ast.2021.107086

Serré, R., Gourdain, N., Jardin, T., Jacob, M. C., & Moschetta, J.-M. (2019). Towards silent micro-air vehicles: Optimization of a low reynolds number rotor in hover. *International Journal of Aeroacoustics*, *18*(8), 690–710. https://doi.org/10.1177/1475472X19890260

Simon, F., Schiller, N. H., Zawodny, N. S., Pettingill, N. A., & Galles, M. B. (2023). Fundamental noise characterization of a ducted propeller in hover. *INTER-NOISE and NOISE-CON Congress and Conference Proceedings*, *265*(7), 657–667. https://doi.org/10.3397/IN_2022_0091

Sinibaldi, G., & Marino, L. (2013). Experimental analysis on the noise of propellers for small UAV. *Applied Acoustics*, *74*(1), 79–88. https://doi.org/10.1016/j.apacoust.2012.06.011

Treuren, K. W. V., & Wisniewski, C. F. (2019). Testing propeller tip modifications to reduce acoustic noise generation on a quadcopter propeller. *Journal of Engineering for Gas Turbines and Power*, *141*(12), 121017. https://doi.org/10.1115/1.4044971

Venkateswaran, R. K., Joseph, P., & Paruchuri, C. C. (2024). Characterizing fan broadband noise using engine intra-stage measurements. *30th AIAA/CEAS Aeroacoustics Conference (2024)*. https://doi.org/10.2514/6.2024-3115

Yilmaz, S., Erdem, D., & Kavsaoglu, M. (2015). Performance of a ducted propeller designed for UAV applications at zero angle of attack flight: An experimental study. *Aerospace Science and Technology*, *45*, 376–386. https://doi.org/10.1016/j.ast.2015.06.005